



Petrography, fluid inclusion, isotope and trace element constraints on the origin of quartz cementation and feldspar dissolution and the associated fluid evolution in arkosic sandstones

Guanghui Yuan, Yingchang Cao, Jon Gluyas, Xu Cao, and Wenbo Zhang

AAPG Bulletin published online June 15, 2017

doi: 10.1306/0608171616017066

Disclaimer: The AAPG Bulletin Ahead of Print program provides readers with the earliest possible access to articles that have been peer-reviewed and accepted for publication. These articles have not been copyedited and are posted “as is,” and do not reflect AAPG editorial changes. Once the accepted manuscript appears in the Ahead of Print area, it will be prepared for print and online publication, which includes copyediting, typesetting, proofreading, and author review. ***This process will likely lead to differences between the accepted manuscript and the final, printed version.*** Manuscripts will remain in the Ahead of Print area until the final, typeset articles are printed. Supplemental material intended, and accepted, for publication is not posted until publication of the final, typeset article.

Cite as: Yuan, G., Y. Cao, J. Gluyas, X. Cao, and W. Zhang, Petrography, fluid inclusion, isotope and trace element constraints on the origin of quartz cementation and feldspar dissolution and the associated fluid evolution in arkosic sandstones, (*in press; preliminary version published online Ahead of Print June 15, 2017*): AAPG Bulletin, doi: 10.1306/0608171616017066.

Copyright © Preliminary Ahead of Print version 2017 by The American Association of Petroleum Geologists

Petrography, fluid inclusion, isotope and trace element constraints on the origin of quartz cementation and feldspar dissolution and the associated fluid evolution in arkosic sandstones

Guanghai Yuan*^{1,2} Yingchang Cao*^{1,2} Jon Gluyas³ Xu Cao⁴ Wenbo Zhang^{1,2}

(1. School of Geoscience, China University of Petroleum, Qingdao, China 266580;

2. Laboratory for Marine Mineral Resources, Qingdao National Laboratory for Marine Science and Technology, Qingdao, 266071, China

3. Department of Earth Sciences, Durham University, Durham, DH1 3LE, UK

4. School of Energy Resources, China University of Geosciences, Beijing, 10083, China)

ACKNOWLEDGMENTS

This study was funded by the Natural Science Foundation of China Project (No. 41602138, No. U1262203), National Science and Technology Special Grant (No. 2016ZX05006-007), China Postdoctoral Science Foundation funded project (2015M580617), and Shandong Postdoctoral innovation project (201502028), and the Fundamental Research Funds for the Central Universities (15CX08001A). Thanks to Shengli Oilfield Company of Sinopec for supplying all samples and some geological data. Red epoxy resin-impregnated thin sections were prepared by Wang Weidong at Zhongyuan Oilfield Company, and doubly polished sections were prepared by Ian Chaplin at Durham University. Petrography and fluid inclusion analysis were made in State key laboratory in China University of Petroleum. Sample preparation and SMIS analysis were conducted with the help of IGGCAS. CL analysis was conducted in Reservoir Geology Key Laboratory of Shandong Province in China University of Petroleum. WDS analysis was conducted in Ocean University of China. AAPG editor Dr. Barry J. Katz, reviewers Dr. Thomas R. Taylor, Dr. Yanzhong Wang and Dr. Jin Lai are thanked for their constructive comments.

ABSTRACT: Feldspar dissolution, quartz cementation, and clay cementation are significant diagenetic processes in deep-water fan feldspar-rich sandstones in the Shengtuo area, Dongying sag (East China). The timing and origin of these water-rock interactions, as well as the paleo-fluids in which relevant chemical reactions occurred were deduced using data from microscopy, fluid inclusion microthermometry, oxygen isotope microanalysis and trace element microanalysis.

Three distinct, separate episodes of quartz overgrowths (referred as Q1, Q2 and Q3) were distinguished by cathodoluminescence (CL) microscopy. Q1 quartz, identified in all porous sandstones from 2500 m (8200 ft) to 3600 m (11800 ft), was formed at approximately 100-115 °C (212-239 °F) before oil filled the reservoirs. Q2 quartz was mainly precipitated at 115-130 °C (239-275 °F), accompanying or slightly postdating the main phase of oil filling, and was identified in samples from 2800 m (9200 ft) to 3600 m (11800 ft). Q3 quartz was only identified in sandstones buried deeper than 3500 m (11400 ft), and was likely precipitated recently when

temperature exceeded 130-135 °C (266-275 °F). Secondary ion mass spectrometry (SIMS) oxygen isotope microanalyses yielded $\delta^{18}\text{O}_{\text{V-SMOW}}$ values ranging from 21.42‰ to 24.35‰ for Q1 quartz, from 22.03‰ to 24.99‰ for Q2 quartz, and from 21.72‰ to 22.91‰ for Q3 quartz.

A mass balance calculation and quantitative petrography data of the amount of leached feldspars and associated secondary minerals suggest that the internal feldspar dissolution is likely the primary source for the authigenic clays and quartz cements in these sandstones. Positive $\delta^{18}\text{O}_{\text{(water)}}$ values (+0.5‰ to +4.5‰ V-SMOW) of quartz-forming waters indicates that quartz cementation and feldspar dissolution occurred in a geochemical system with a limited volume of diagenetically modified connate water. The variations of $\delta^{18}\text{O}_{\text{(cements)}}$ and trace element compositions from Q1 quartz to Q2 quartz in individual overgrowth suggest that hydrocarbon filling changed the chemistry of the pore fluid significantly; further, $\delta^{18}\text{O}_{\text{(water)}}$ values of the pore water increased by about 2‰ V-SMOW after oil filling.

Meteoric freshwater did not contribute to quartz cementation and simultaneous feldspar dissolution. The detected CO_2 and hydrocarbons in fluid inclusions in the quartz cements, the existence of CO_2 in hydrocarbon-rich natural gas and the bitumen in the feldspar-hosted pores suggest that acids derived from organic matter (kerogen in source rocks and hydrocarbons in reservoirs) probably have promoted the extensive subsurface leaching reactions of feldspars in these sandstones. The ongoing development of Q2 and Q3 quartz suggested that quartz precipitation did not cease after oil filling. Further, diagenetic reactions likely have proceeded from water-rock interactions to hydrocarbon-water-rock interactions.

Key Words: Quartz cementation; Subsurface feldspar dissolution; Fluid inclusion; Oxygen isotope; Secondary ion mass spectrometry (SIMS); Trace element.

1 Introduction

Evaluating the timing and origin of water-rock interactions, and paleo-fluid in which relevant mineral cementation and dissolution occur is critical with regard to understanding the evolution of porosity in sandstone reservoirs during burial (Harwood et al., 2013; Pollington et al., 2011; Taylor et al., 2010). Feldspar dissolution and precipitation of authigenic quartz and clays are significant diagenetic reactions affecting the reservoir quality of feldspar-rich sandstones (Glasmann, 1992; Yuan et al., 2015a; Zhu et al., 2010). Secondary pores formed by feldspar dissolution (i.e., feldspar-hosted pores) are likely to dominate pore spaces in moderately-deeply buried sandstones (Dutton and Loucks, 2010; Yuan et al., 2015a; Lai et al, 2017); therefore, understating the origin of these secondary pores and associated secondary minerals is especially necessary for an accurate evaluation of reservoir quality.

Though a dozen hypotheses have been proposed to interpret secondary pores in subsurface sandstones since the 1970s (Hutcheon et al., 1993; Schmidt and McDonald, 1979; Smith and Ehrenberg, 1989; Surdam and Boese, 1984), some older research (Giles and Marshall, 1986; Lundegard et al., 1984) and recent reviews (Bjørlykke, 2014; Taylor et al., 2010) suggested that these hypotheses (including the organic CO_2 -leaching theory and organic acid leaching hypothesis) cannot be used to explain the formation of massive subsurface secondary porosity (eg. >5%) in buried sandstones, due to the supposed extensive consumption of these acids by carbonate minerals in the source rocks. Based on studies of petrography, isotopic composition of CO_2 gas and carbonate

cements, and numerical simulations of water-rock interactions in a CO₂-feldspar-calcite-H₂O system with constraints of pore water and CO₂ partial pressure, it has been proposed that the CO₂ acid from kerogen maturation selectively dissolves large amounts of silicate minerals (e.g. feldspar) but not carbonate minerals in moderately-deeply buried geochemical systems with a limited volume of pore water (Jia et al., 2016; Yuan et al., 2015b). Carbonate dissolution in a closed geochemical system is suppressed due to the low equilibrium constant of the carbonate leaching reaction.

Secondary pores formed by dissolution of detrital feldspars do not preserve the geochemical identity of the pore water that have caused the dissolution reaction, making it challenging to identify the paleo-fluid that was responsible for the leaching reaction. Oxygen isotopic compositions, trace elements and fluid inclusions in authigenic minerals can provide insight into the paleo-fluid evolution during diagenesis, and are critical to understand the cementation history (Aplin and Warren, 1994; Girard et al., 2001; Lehmann et al., 2011; Pollington et al., 2011; Williams et al., 1997). $\delta^{18}\text{O}_{(\text{cements})}$ and trace element compositions of quartz cements in quartzose sandstones with large amounts of quartz cements have been studied in many cases (Harwood et al., 2013; Lehmann et al., 2011; Pollington et al., 2011), and pressure dissolution of quartz grains generally dominate the silica source of the quartz cements (Mcbride, 1989; Worden and Barclay, 2000). Unlike the quartzose sandstones (Pollington et al., 2011; Walderhaug, 1996, 2000), the amount of quartz cements in subsurface lithic arkose and feldspathic litharenite sandstones is generally less than a few percent (Higgs et al., 2007; Mcbride, 1989; Yuan et al., 2013). The pressure dissolution of detrital quartz grains in the originally feldspar-rich sandstones is generally weak (Glasmann, 1992; Worden and Barclay, 2000), particularly when strong fluid overpressure develops and forestalls the onset of pressure solution (Yuan et al., 2015a; Taylor et al., 2010). Previous studies suggested that internal feldspar dissolution might dominate the silica source of the quartz cements in the feldspar-rich sandstones (Barclay and Worden, 2000; Glasmann, 1992; Higgs et al., 2007; Worden and Barclay, 2000; Yuan et al., 2015c). Thus, studies of the quartz cements in feldspar-rich sandstones may provide distinct insight into the simultaneous feldspar dissolution. To date, however, there are few studies on coupled micro-analysis of petrography, fluid inclusion, isotope and trace elements within quartz cements in feldspar-rich sandstones.

Feldspar-rich sandstones in deep-water sublacustrine fans in the Shengtuo area, Dongying sag, East China have experienced extensive subsurface leaching of detrital feldspars, and quartz cements precipitated mainly as overgrowths on detrital quartz grains or as some quartz crystals in pores (Yuan et al., 2015c; Zhang et al., 2014). General diagenesis and reservoir quality of such sandstones have been reported in previous studies (Yuan et al., 2015c; Zhang et al., 2014), and feldspar dissolution was suggested to be the primary silica source of the quartz cements using quantitative petrography data (Yuan et al., 2015c). In the present study, three distinct, separate episodes of quartz overgrowths were identified in the sandstones, using cathodoluminescence (CL) microscopy. Given that the size of the quartz overgrowth is thick enough for the micro-analysis of oxygen isotope composition and trace elements, and that the quartz overgrowths have encapsulated some inclusions of the paleo-fluids from which the quartz cements were precipitated, this represents a novel opportunity to study the detailed evolution of quartz cementation and the origin of paleo-fluids related to the water-rock interactions. In

this study, a micro-analysis of petrography, homogenization temperature (T_h) of the aqueous fluid inclusions, in situ $\delta^{18}\text{O}_{(\text{quartz})}$ values and wavelength dispersive spectroscopy (WDS) elements within quartz overgrowths, and CO_2 data in natural gas from the sandstone reservoirs were combined to thoroughly decipher the evolution of the three stages of quartz cementation, associated feldspar diagenesis, and relevant paleo-fluids.

The main aims of this article are to: (1) identify the diagenetic mineral assemblage relevant to the feldspar diagenesis in deep-water fan sandstones without incursion of meteoric freshwater; (2) investigate the formation temperature, the silica source, and the nature of the paleo-fluids for the three episodes of quartz cements; and (3) identify the timing of the feldspar leaching reactions and possible corrosive fluids that have promoted the subsurface feldspar dissolution using the geochemical information from the relevant authigenic minerals.

2 Geological background

The Dongying sag, an important hydrocarbon-producing subunit of Bohai Bay Basin, is located on the eastern coast of China and covers an area of approximately 5700 km^2 (2200 mi^2) (Figure 1) (Guo et al., 2012). It is a rift lacustrine basin developed in the Late Jurassic to the early Cenozoic on the basement of the North China Platform. The Dongying sag is further subdivided into five secondary tectonic zones from the north to the south. The Shengtuo area, with an exploration area of 230 km^2 (90 mi^2), includes the middle part of the northern steep slope zone and the Lijin subsag (Figure 1B) (Yuan et al., 2015a).

From base to top, the sediments deposited in the Shengtuo area are represented by the Kongdian (Ek), Shahejie (Es), the Dongying (Ed), Guantao (Ng), Minghuazhen (Nm), and Pingyuan (Q) Formations. Regional uplift in the late Oligocene created an unconformity between the Ed and Ng Formations. The Shahejie Formation, which contains the main source rocks and reservoir rocks, is divided into four members, Es1, Es2, Es3 and Es4 (from top to base) (Figure 2) (Yuan et al., 2015a). The Es3 member can be subdivided into three submembers of Es_3^1 , Es_3^2 , Es_3^3 , and the Es4 members can be subdivided into two submembers including Es_4^1 and Es_4^2 (from top to base).

The sandstone samples used in this study were selected from the deep-water sublacustrine fans deposited in the Es_3^2 , Es_3^3 , and Es_4^1 submembers. In the Shengtuo area, the Es_3^2 , Es_3^3 , and Es_4^1 sub-members are comprised of thick organic-rich brownish gray, or gray to black mudstones, shales, oil shales, calcareous mudstones, dolomites, and sandstones wrapped in these thick mudstones or shales (Cao et al., 2014), with a high mud/sand ratio ranging from 10:1 to 30:1 (Figure 3).

The burial and thermal history of the northern Dongying sag have been analyzed in detail (Song et al., 2009; Guo et al., 2010; Cao et al., 2014). The present-day geothermal gradient is around $34 \text{ }^\circ\text{C}/\text{km}$ ($98 \text{ }^\circ\text{F}/\text{mi}$), with an average earth surface temperature of $14 \text{ }^\circ\text{C}$ ($57 \text{ }^\circ\text{F}$) (Guo et al., 2010); the sandstones in the Shahejie Formation are currently at their maximum burial depth and temperature. The main source rocks have a total organic carbon content (TOC) ranging from 0.5% to 18.6% with an average of 5%, and the average vitrinite reflectance varies from 0.35% to 1.5% from 2000 m (6560 ft) to 5000 m (16400 ft), indicating that they are immature to mature (Guo et al., 2012). The Shengtuo area grows increasingly to be moderately to strongly over-pressured as the depth increases. The pressure coefficient (the ratio between tested fluid pressure and hydrostatic pressure) ranges from 1.2 to 1.8 in the sandstone reservoirs from 2200 m (7200 ft) to 5000 m (16400 ft) (Guo et al., 2010; Yuan

et al., 2015a).

3 Data base and methods

Fluid pressure data and natural gas composition data of 19 samples from the Es₃²-Es₄¹ sandstone reservoirs in the Shengtuo area were collected from the Shengli Oilfield Company of Sinopec. Forty medium- to coarse-grained sandstones and pebbly sandstones with a small amount of clay matrix were collected from ES₃²-Es₄¹ cores of 17 wells (Figure 1B). Forty-five red epoxy resin-impregnated thin sections and 20 scanning electron microscopy (SEM) samples were examined with optical, reflected, cathodoluminescence (CL), and scanning electron microscopy to identify the diagenesis and petrography textures of the leached feldspars, authigenic quartz, kaolinite, illite, and carbonate cements. Quantitative work was conducted on thin sections with low content of detrital clays to obtain the amount of different minerals and various pores in the sandstones. Point-counts were performed for detrital compositions with at least 300 points, which can provide a standard deviation of approximately 6% (Van der Plas and Tobi, 1965). The amount of secondary pores and authigenic cements in the thin sections were obtained using a quantitative image analysis method described by Yuan et al (2015a), with the help of microscope and Image-Pro Plus software. The errors obtained by using this quantitative image analysis method are generally less than 0.5%, 0.2%, and 0.1% when the test data range from 2% to 4%, 0.5% to 2%, and 0 to 0.5%, respectively (Yuan et al., 2015a).

The optical and reflected microscopy analysis was conducted using a Zeiss microscope. The SEM samples were identified utilizing a Quanta200 SEM combined with an EDAX Energy dispersive spectroscope. CL images were collected using a CL 8200 MK5 detector on a Zeiss microscope with an accelerating voltage of 15 kV. After examining the thin sections, we selected ten rock chips with quartz overgrowths to make 100 μm thick, double-polished sections for fluid inclusion and δ¹⁸O composition analysis. The ten sandstone samples were collected from four drilling cores, with a burial depth ranging from 2700 m (8850 ft) to 3900 m (12800 ft). UV light was used to identify aqueous or hydrocarbon fluid inclusions with an Axioskop 40 microscope (Carl Zeiss). The microthermometry of the aqueous inclusions was conducted using a calibrated Linkam TH-600 stage, and the homogenization temperature (T_h) was obtained by cycling. T_h values were measured under a heating rate of 10 °C/min (18°F/min) when the temperature was lower than 70 °C (158 °F) and a rate of 5 °C/min (9 °F/min) when the temperature exceeded 70 °C (158 °F). The measured temperature precision for T_h is ±1 °C (±1.8 °F).

Areas of the rocks with some thick quartz overgrowths (>25 μm wide) were identified using optical and reflected microscopy. These areas were then cored out from the doubly polished thin sections, then mounted into three blocks alongside international NBS-28 standard quartz grains (with δ¹⁸O_{V-SMOW} value of +9.6‰) and laboratory Qinghu standard quartz grains (+8.4‰ V-SMOW). Micrographs of these three specimen blocks were, as mentioned above, captured with optical, reflected and cathodoluminescence (CL) microscopy to select the ion microprobe spots. In situ secondary ion mass spectrometry (SIMS) oxygen isotopic composition analysis of the detrital quartz and the quartz overgrowths in four sandstone samples and the standard quartz was performed using a CAMECA IMS-1280 ion microprobe at the institute of Geology and Geophysics, Chinese Academy of Sciences (IGGCAS) in Beijing. The measurements were performed by using a ≈ 1.18 nA defocused primary ion beam of Cs⁺ (impact energy 10 KeV) producing circular ablation craters of approximately 15 μm in diameter.

Positive charge buildup on the sample was neutralized by using of a normal incidence electron flood gun. The analytical procedures were similar to those reported by Li et al., 2013. The samples after isotope analysis were examined again using optical and reflected microscopy to identify the location of the craters, and CL was used to identify the phases of the quartz overgrowths that had been tested. The internal precision of the $^{18}\text{O}/^{16}\text{O}$ ratios is ca. 0.2‰ (2 standard deviations, 2SD) from 20 cycles of measurements (Li et al., 2012). The results of 69 analyses of NBS-28 standard quartz are shown in Figure 4. The data show a total range of 9.24‰ to 9.94‰ and yield an average $\delta^{18}\text{O}$ value of $9.60 \pm 0.3\text{‰}$ (2SD) (Figure 4). Detailed values of the $\delta^{18}\text{O}_{(\text{NBS-28})}$ compositions are provided in Appendix Table 1.

After selecting points for areas of interest in the quartz minerals, a wavelength dispersive spectroscopy analysis was performed using a JXA-8230 SEM with wavelength dispersive spectrometers located at the Ocean University of China. The trace elements measured in the quartz overgrowth and the concentric bands included Al, Na, Mg, K, Ca, Ti, Fe, Cr, and Mn. Analysis times were 100 seconds on each peak and 50 seconds on each background. The accelerating voltage was 15 kV, the beam current 20 nA, and the circle probe size was 5 μm . The employed standards were SRM-1212 for Al, Na, K, and Ca, MgO for Mg, TiO_2 for Ti, Cr_2O_3 for Cr, and manganese metal for Mn. Limits of detection (3 sigma) are: 138 ppm for Al, 122 ppm for Na, 118 ppm for Mg, 105ppm for K, 119 ppm for Ca, 227 ppm for Ti, 195 ppm for Fe, 209 ppm for Cr, and 207 ppm for Mn.

4 Results

4.1 Sandstone petrography and diagenesis

Yuan et al. (2015c), Cao et al. (2014), and Zhang et al. (2014) have provided detailed descriptions of the sedimentary facies and diagenetic transformations of the sandstones in this study. The main features of relevance are summarized below (Figure 5) (Cao et al., 2014; Yuan et al., 2015c; Zhang et al., 2014).

The analyzed sandstones are clean moderately-sorted lithic arkoses and feldspathic litharenites, with an average framework composition of $\text{Q}_{34}\text{F}_{42}\text{R}_{19}$ and less than 1% detrital clays (Table 1). The composite diagenetic sequences, as previously reported, include compaction and early carbonate cementation in the eodiagenetic stage, subsequent dissolution of feldspars, precipitation of kaolinite and quartz, late carbonate cementation, and illitization of kaolinite and feldspars in the mesodiagenetic stage (Yuan et al., 2015b, c) (Figure 5). Unlike quartzose sandstones (Walderhaug, 1996, 2000), petrography textures suggest that the pressure dissolution of detrital quartz is rather weak in these feldspar-rich sandstones with a strong fluid overpressure (Figure 6; Figure 7). Sandstones at the margin of sandstone beds were extensively cemented by early carbonate cements, exhibiting very low porosity (<10%) (Figure 6A); leached feldspars, authigenic quartz, and clays are generally scarce in such sandstones (Figure 6A; Table.1). The diagenesis in porous sandstones at the central part of the sandstone beds is more complicated. Porous sandstones commonly do contain feldspar-hoted pores, authigenic quartz, clays, and some late carbonate cements that developed during deep burial (Figure 6B-K) (Yuan et al., 2015c).

The feldspar diagenesis significantly altered the composition of the sandstones. The feldspar compositions, including mainly detrital K-feldspar grains and K-feldspar in polymineralic rock fragments, can be identified as being partially to fully dissolved (Figure 6B-H). Monocrystalline or polycrystalline feldspar grains may be

dissolved fully, though most of the feldspars are only partially dissolved. The internal fabric of the feldspar is still recognizable by intricate structures consisting of remnants and secondary pores. The partial dissolution may be due to varying compositions or limited leaching time. Some detrital plagioclase grains can be identified to be partially leached, but this is not common. In thin sections, the amount of feldspar-hosted pores can reach up to 2-3% of the total rock, with an average around 1.5% (Table.1). These secondary pores play an important role in reservoirs and residual bitumen and oil can be identified in certain feldspar-hosted pores in the thin sections without oil removal (Figure 6H, I).

The authigenic quartz in porous sandstones occurs mainly as syntaxial quartz overgrowths on detrital quartz grains (Figure 7) and microcrystalline quartz in pores (Figure 8D). Quartz overgrowths are typically 20-50 μm wide, with some reaching up to 100-120 μm in width. In most cases, quartz overgrowths can be easily identified with optical and reflected microscopy by dust rim or fluid inclusions at the grain-overgrowth boundary (Figure 7A, B, C, D). Early petrographic investigations identified the presence of two phases of diagenetic quartz, using only optical microscopy (Yuan et al., 2015c). In the present study, three distinct phases of quartz overgrowths were unambiguously identified using cold CL microscopy, and the diagenetic quartz phases grew more abundant as the burial depth increased (Figure 7). In thin sections, the amount of quartz overgrowths can reach up to 1% of the total rock (Table.1, Figure 9B).

The three phases of quartz overgrowths identified under the CL microscope are referred as Q1, Q2 and Q3. Only Q1 was identified in the porous sandstones at depths of 2500 m (4530 ft) to 2800 m (5070 ft), and it exhibited a dull, gray-black luminescence. In the porous sandstones at depths of 2800 m (5070 ft) to 3500 m (6330 ft), both Q1 and Q2 quartz phases were identified, and Q2 quartz exhibited a brown gray luminescence (Figure 7B-C'). The co-existence of Q1, Q2, and Q3 was only identified in the samples buried deeper than 3500 m (6330 ft) (Figure 7D, D'). Q3 quartz also exhibited a dull, gray black luminescence almost identical to Q1. Q2 quartz can be identified as directly precipitated on detrital feldspar grains (Figure 7B, B'). The Q1/Q2/Q3 boundaries were sharp and linear, reflecting euhedral morphology and, therefore, the diagenetic origin of Q1 (Figure 7C', D'). Residual bitumen or oil was found locally trapped between Q2 and Q1 or between Q2 and the detrital grains (Figure 10A-D), indicating that a phase of oil filling occurred in between the two phases of quartz cementation.

Authigenic clays are common in the sandstones with extensive feldspar dissolution. The authigenic clays in the sandstones are mainly kaolinite and illite (Figure 8). No authigenic chlorite was identified and no chlorite coating developed on the quartz surfaces in the marginal sandstones or the central sandstones. The authigenic clays occurred mainly as kaolinite in sandstones buried shallower than 3100 m (10170 ft) (Figure 6D, J; Figure 8B-D) and mainly as illite in sandstones buried deeper than 3100 m (10170 ft) (Figure 6K; Figure 8E, F) (Yuan et al., 2015a). Kaolinite occurred as euhedral booklets and vermicular aggregates, and illite occurred primarily as fibrous crystals (Figure 8). In thin sections, the amount of clays can reach up to 3% of the total rock (Table.1; Figure 10A).

The authigenic quartz and clay are scarce in porous sandstones with relatively weak feldspar dissolution (Figure 6L). Extensive feldspar dissolution, however, was commonly accompanied by precipitation of abundant authigenic clays and quartz cements in nearby primary pores (Figure 6D; Figure 8A). The mixtures of the

authigenic clays and the quartz cements (Figure 8B, D) indicate the likely simultaneous precipitation of these cements. Our quantitative petrographic data (Table 1) shows a positive linear relationship between the amount of feldspar-hosted pores and that of the authigenic clays and quartz cements (Figure 9).

4.2 Fluid inclusions

The type of fluid inclusions preserved in various quartz minerals (grains or different phases of quartz overgrowths) were identified using UV light and CL microscopy (Figure 10). Secondary fluid inclusions in healed microfractures in quartz grains are abundant, while primary fluid inclusions in quartz overgrowths (particularly aqueous inclusions) are much less common. Both aqueous and oil fluid inclusions developed in healed microfractures in the quartz grains. Only aqueous fluid inclusions were identified in Q1 quartz (Figure 10C, D, E, F), while oil fluid inclusions (OFI) are generally more abundant than aqueous fluid inclusions in Q2 quartz (Figure 10C, D, G, H).

The size of tested aqueous fluid inclusions ranges mainly from 3 μm to 8 μm (Table 2). After measuring the homogenization temperature (T_h), CL microscopy was employed to identify quartz overgrowth phases. The test data shows that the T_h of the aqueous inclusions in Q1, Q2 and Q3 quartz ranges mainly from 100 °C (212 °F) to 115 °C (239 °F), 115 °C (239 °F) to 130 °C (266 °F), and 134 °C (273 °F) to 138 °C (280 °F) (only three data points available), respectively (Figure 11, Table 2).

4.3 In situ isotopic compositions of quartz overgrowths

Four samples were investigated by using secondary ion mass spectrometer (SIMS). A total of 197 microanalyses were performed for different detrital and authigenic quartz sites (Figure 12, Appendix Table 2), which were carefully selected in thin sections on the basis of sufficient widths ($>25 \mu\text{m}$) of the quartz overgrowths for the SIMS analysis, and the visible boundary (dust rim or fluid inclusions) between the grain and the overgrowth. After ion microprobe analysis was complete, all analysis pits were examined by optical, reflected, and CL microscopy to determine the exact locations of the SIMS ion microprobe pits and the nature of the quartz (Figure 13): detrital quartz grains, different phases of quartz overgrowths, or a mixture. The $\delta^{18}\text{O}$ values of the analyzed four rocks are shown in histogram form (Figure 12). $\delta^{18}\text{O}_{\text{V-SMOW}}$ values within the quartz grains ranges mainly from 8‰ to 13‰; $\delta^{18}\text{O}_{\text{V-SMOW}}$ values of the combination of detrital and authigenic quartz have a wide range from 13‰ to 24‰; $\delta^{18}\text{O}_{\text{V-SMOW}}$ values of pure authigenic Q1, Q2 and Q3 quartz range mainly from 21.42‰ to 24.35‰, 22.03‰ to 24.99‰, and 21.72‰ to 22.91‰, respectively (Figure 12). Detailed values of the $\delta^{18}\text{O}_{\text{(cement)}}$ compositions are provided in Appendix Table 2.

Detailed transverse were measured on certain thick individual overgrowths to investigate the evolution of $\delta^{18}\text{O}_{\text{(cement)}}$ within the quartz overgrowths (Figure 13). In a thick Q1 quartz overgrowth, $\delta^{18}\text{O}_{\text{(cement)}}$ values in individual quartz overgrowths generally decrease from the inner part to the outer edge (Figure 13A-A'', B-B''). In a thick quartz overgrowth including Q1, Q2, and (or) Q3, $\delta^{18}\text{O}_{\text{(cement)}}$ values decrease in Q1 quartz, while $\delta^{18}\text{O}_{\text{(cement)}}$ values in Q2 quartz exhibit a decrease or an almost stable pattern (Figure 13C, C'', D, D''). From Q1 to Q2, there was an increase of the $\delta^{18}\text{O}_{\text{(cement)}}$ values. From Q2 to Q3 quartz, there is a decrease of $\delta^{18}\text{O}_{\text{(cement)}}$ values (Figure 13D-D'').

4.4 Wavelength dispersive spectroscopy data

Wavelength dispersive spectroscopy (WDS) analysis was conducted on detrital and authigenic quartz samples from the sandstones to obtain their chemical compositions. Trace elements data (in mass percent) of one quartz overgrowth with Q1, Q2 and Q3 quartz at a depth of 3535 m (11598 ft) in well Tuo720 was reported here in traverses from detrital quartz grains to quartz overgrowth (Figure 14, Table 3). The trace elements with the highest concentration are Al, followed by Ca, Fe, K, and Mn. The trace element concentrations are generally much lower for the detrital quartz grain than for the quartz overgrowth.

The WDS profile from the Q1 quartz to the Q3 quartz overgrowths shows great significant variations in the content of aluminium and manganese. Q1 and Q3 quartz contain more aluminium than Q2 quartz, while Q2 quartz has more manganese than Q1 and Q3 quartz. The WDS trace element microanalysis yielded an Al₂O₃ content ranging from 0.046% to 0.156% for Q1 quartz, from 0 (not detected) to 0.086% for Q2 quartz, and from 0.156% to 0.170% for Q3 quartz, respectively; the MnO content ranges from 0 to 0.005% for Q1 quartz, from 0.01% to 0.026% for Q2 quartz, and from 0 to 0.012% for Q3 quartz, respectively. Almost all quartz overgrowths contain some Ca, K, Fe and Mg. Ti and Cr, however, can only be detected in the Q1 quartz and the Q3 quartz, respectively.

4.5 Natural gas composition and CO₂ partial pressure

Natural gas produced from the Shengtuo deep-water fan sandstone reservoirs is hydrocarbon-rich gas composed of methane (45.8-89.2%), ethane (1.5-13.1%), propane (0.6-16.8%), butane (0-12%), CO₂ (1.92-12.19%), and minor higher hydrocarbons (Table 4). The CO₂ partial pressure (pCO₂) in the sandstone reservoirs was calculated using the method described in Smith and Ehrenberg (1989) with the tested fluid pressure and the mole content of CO₂ in these natural gas, and the pCO₂ in the sandstone reservoirs ranges from 7.2 bar (0.72MPa) to 56.8 bar (5.68MPa).

5 Discussion

5.1 Quartz cementation temperature

The aqueous inclusions tested in the present study were located within the quartz overgrowths, resetting and leakage as a result of subsequent burial are unlikely (Girard et al., 2001); the spherical or elliptical shape of the aqueous inclusions further supports this suggestion (Figure 10). As CH₄ and CO₂ were detected in the two phase aqueous inclusions in the sandstones by Raman spectrometry (Chen et al., 2010), the measured T_h is likely close to the trapping temperature.

Quartz cementation in most sandstones generally occurs when the formation temperature exceeds 70-80 °C (158-176 °F) (Girard et al., 2001; McBride, 1989; Robinson and Gluyas, 1992; Walderhaug, 2000; Worden and Morad, 2000). Without strict constraints of pore water δ¹⁸O composition, however, recent in situ δ¹⁸O data of quartz cements have been used to suggest a much lower threshold temperature (10-70 °C (50-158 °F)) for quartz cementation in quartz-rich sandstones (Harwood et al., 2013; Kelly et al., 2007). The T_h values of the aqueous inclusions occurring within the very beginning of the quartz overgrowths in the studied feldspar-rich sandstones are generally not lower than 95-100 °C (203-212 °F) (Figure 11, Table 2), which suggests that quartz cementation in this set of feldspar-rich sandstones probably began to occur at relatively high temperatures.

With no development of oil inclusions in Q1 quartz, the T_h data of Q1 aqueous inclusions indicates that Q1 quartz formed at approximately 100-115 °C (212-239 °F) before oil filling (Figure 11). With both aqueous and oil fluid inclusions in Q2 quartz, the T_h data of Q2 aqueous inclusions indicates that Q2 quartz mainly precipitated at 115-130 °C (239-266 °F), accompanying or slightly postdating the main phase of oil filling. As it was identified only in deeply buried sandstones, Q3 likely formed relatively recently when formation temperature exceeded 130 °C (266 °F). The T_h values of the aqueous inclusions within the inner part of the different quartz overgrowths exhibits large differences (Table 2), indicating that the initial precipitation of individual quartz overgrowths on different grains probably began at different temperatures. The direct precipitation of Q2 quartz on detrital quartz grains (Figure 7B, B') also demonstrates that quartz cementation did not occur homogeneously on all detrital grains. Any heterogeneity of these diagenetic reactions, even on a small geochemical scale, may be due to the heterogeneity of quartz grains or the chemistry of pore fluids (French, 2012; Taylor et al., 2010). The absence of quartz cements in marginal low porosity sandstones with extensive carbonate cementation (which occurred at 35-70 °C (95-158 °F) (Yuan et al., 2015c)) and the floating texture of detrital grains identified in the thin sections (Figure 6A) also suggest that quartz cementation did not occur at lower temperatures. The phases of authigenic quartz are more abundant as the burial depth increases (Figure 7), and the T_h of aqueous inclusions in quartz cements may reach up to the present-day formation temperature in certain samples (Figure 11), indicating that the quartz cementation has not only likely continued to the present time but may still be on-going in some places.

5.2 Timing of feldspar leaching

The timing of feldspar dissolution in sandstones could be early synsedimentary, associated with unconformities, or taking place during later burial (Bjørlykke and Jahren, 2012; Molenaar et al., 2015).

Although secondary pores formed as a result of detrital feldspar dissolution do not directly preserve the geochemical identity of the paleo-fluids that have caused the dissolution, several lines can be used to investigate the relative timing of the feldspar dissolution. Firstly, the feldspar dissolution occurred mainly in porous sandstones (Figure 6), whereas the low porosity sandstones with abundant early-diagenetic carbonate cements generally contain very limited feldspar-hosted pores (Figure 6A), indicating that the extensive feldspar dissolution occurred mainly after early eodiagenetic carbonate cementation (Yuan et al., 2015c). The oxygen isotopic compositions of the carbonate minerals (Yuan et al., 2015c) and the petrographic texture of point contacts of the detrital grains or the floating textures (Figure 6A) in the sandstones confirm this idea. Secondly, oversized pores from early shallow dissolution of grains would have been destroyed by framework collapse during deep burial (Wilkinson et al., 2001), and early formed authigenic clay fabrics would also have been deformed by later compaction (Molenaar et al., 2015). However, in the present sandstones, the secondary pores have preserved the original outlines of former grains (Figure 6D-G), and the associated authigenic kaolinite and illite are unaffected by deep burial compaction and still maintain pseudo hexagonal, vermicular or fibrous shapes (Figure 8). We do not exclude the early synsedimentary or shallow leaching reactions. These petrography textures (Figure 6), however, suggest that the feldspar dissolution in the sandstones we examined probably occurred mostly after the eodiagenetic stage, during which time compaction and early-diagenetic cementation

dominated.

Feldspar dissolution is a kinetically controlled mineral reaction and its dissolution rate is affected by available feldspar surface, temperature, water pH, saturation state (controlled by concentration of $\text{SiO}_2(\text{aq})$, Al^{3+} , and K^+ or Na^+ in pore water), and precipitation rate of secondary minerals (clays and quartz) (Fu et al., 2009; Kampman et al., 2009; Thyne et al., 2001). Laboratory feldspar dissolution experiments demonstrate that the rate constants for feldspar dissolution increase by a factor of about hundreds to ten thousand as the temperature increases from 20 °C (68 °F) to 120 °C (248 °F) (Thyne et al., 2001) or as fluid pH decreases from 7-8 to 4-5 (Kampman et al., 2009). In the eodiagenetic stage when the sandstone geochemical system was characterized by neutral to weak alkaline connate pore water (Wang et al., 2013) and low temperature, as the petrography textures (Figure 6A) suggested, the feldspar dissolution during this period was relatively weak. During the mesodiagenetic stage, the high CO_2 partial pressure (Table 4) in the sandstone geochemical system with silicate and carbonate minerals would reduce the pore water pH to 4-5 (Yuan et al., 2015b). With high temperature and low pH corrosive fluids charged with acids, it is likely that extensive leaching of feldspars probably occurred during the mesodiagenetic period (Thyne et al., 2001; Kampman et al., 2009). As suggested by the T_h of the aqueous inclusions in quartz overgrowths (Figure 11), the dissolution of feldspars and the precipitation of clays and quartz may still be active to date. The dissolution-precipitation processes probably reached a metastable equilibrium state after long term contact between the pore water and the minerals (Giles and De Boer, 1990), and the precipitation rates of relevant secondary minerals likely dominates the feldspar leaching reaction by controlling the consumption of the solutes released by the feldspar dissolution (Alekseyev et al., 1997; Zhu et al., 2004; Zhu et al., 2010; Zhu and Lu, 2009).

5.3 Silica for quartz cements

Internal silica sources including biogenic silica, pressure dissolution of detrital quartz, feldspar dissolution, and external silica sources as clay-mineral reactions in interbedded mudstones have been suggested for quartz cements in sandstones (Alekseyev et al., 1997; McBride, 1989; Walderhaug, 2000).

Sands containing biogenetic silica generally are deposited in marine environments, whereas the Shengtuo sandstones are sediments of gravity flows deposited in a deep lake; no trace of biogenetic silica has been identified in these sandstones (Figure 6). Further, petrography shows little evidence of pressure dissolution of detrital quartz grains (Figure 7; Figure 13) in these sandstones, excluding it as a primary internal silica source.

In the porous sandstones we examined, abundant authigenic clays and quartz cements in thin sections were generally accompanied by extensively leached feldspars (Figure 6D; Figure 8A), and samples with weak feldspar dissolution contained very few authigenic clay and quartz cement (Figure 6L). The positive linear relationship between the amount of feldspar-hosted pores and relevant secondary minerals (Figure 10) demonstrates that feldspar dissolution is probably the most important silica source for quartz overgrowths in the sandstones we examined (Yuan et al., 2015a). A mass balance calculation based on coupled feldspar dissolution and associated mineral precipitation reactions suggested that the expected volume of secondary minerals from the leached feldspars in the sandstones is similar to the amount of authigenic kaolinite and quartz cement identified in the sandstones (Table 1; Figure 9), indicating that the feldspar dissolution could account for the solutes needed for

the precipitation of these authigenic minerals. Chlorite clay coatings did not exist on the quartz grain surfaces. The entire process from feldspar dissolution to precipitation of clays and quartz probably occurred on a thin section scale, and diffusion probably dominated the transfer of silica released from leached feldspars to the precipitation sites (Stoessel, 1987). The amount of aluminum and potassium detected in the quartz overgrowths are much higher than in the detrital quartz grains (Figure 14), which also suggests that the feldspar dissolution reaction that released solutes including aluminum, potassium, and silica is likely the most important silica source for the quartz cementation.

The marginal sandstones with large amounts of early stage diagenetic carbonate minerals are characterized by low porosity and permeability, weak feldspar dissolution and quartz cementation. Such marginal sandstones with low permeability could act as barriers between the mudstones and the central sandstones (Saigal and Bjørlykke, 1987). Though clay XRD data in mudstones suggests that a smectite-to-illite reaction could release silica (Yuan and Wang, 2001), the feldspar dissolution in sandstones could also release large amounts of silica. The concentration difference of $\text{SiO}_2(\text{aq})$ between the mudstone system and the sandstone system should be low (Thyne, 2001). With low porosity and a low gradient of $\text{SiO}_2(\text{aq})$ concentration, an extensive diffusion of $\text{SiO}_2(\text{aq})$ from the mudstone to the interbedded sandstones is not likely to occur (Bjørlykke, 2011), which is also verified by the distribution of relatively few quartz cements in the marginal sandstones and more quartz cements in the central sandstones of individual sandstone beds (Yuan et al., 2015c).

5.4 Paleo-fluids for quartz cementation and feldspar dissolution

Because the quartz cementation occurred simultaneously with the main feldspar dissolution in these feldspar-rich sandstones, the geochemical data preserved in the quartz cements can be used to investigate the paleo-fluids in which these diagenetic interactions occurred.

5.4.1 Pore water for quartz cementation and feldspar dissolution

The $\delta^{18}\text{O}_{(\text{water})}$ values of the lake water in the Dongying sag during the deposition period of the Es4 member has been estimated as approximately -4‰ V-SMOW, using oxygen isotopic composition of sedimentary carbonates in calcareous mudstones (Yuan et al., 2015c). With constraints of the precipitation temperatures derived from aqueous inclusions in quartz overgrowths and the $\delta^{18}\text{O}$ values of the quartz overgrowths, we calculated the oxygen isotopic compositions of paleo-fluids in which quartz cements were formed, using the quartz-water oxygen isotope fractionation equation (Figure 15) (Méheut et al., 2007). The $\delta^{18}\text{O}_{(\text{water})}$ values of the paleo-fluid from which Q1 precipitated were estimated to range from +0.5‰ to +1.5‰ V-SMOW (Figure 15). Accordingly, the $\delta^{18}\text{O}_{(\text{water})}$ values of pore water evolved to become heavier from the eodiagenetic stage to the mesodiagenetic stage. Recrystallization reactions of clay minerals and carbonate minerals and kerogen degradation in the source rocks tend to account for such an enrichment of the $\delta^{18}\text{O}$ composition (Fayek et al., 2001; Wilkinson et al., 1992).

Q1 quartz was formed mainly from 100 °C (212 °F) to 115 °C (239 °F), and the $\delta^{18}\text{O}_{(\text{cement})}$ values decrease with the continuous growth of these overgrowths (Figure 13A'', B''). Though feldspar dissolution and precipitation of quartz and kaolinite in the sandstone itself may decrease the $\delta^{18}\text{O}_{(\text{water})}$ values to some extent (Girard et al., 2001), the water-rock interactions in the associated mudstones (Fayek et al., 2001; Wilkinson et al.,

1992) can keep the $\delta^{18}\text{O}_{(\text{water})}$ value stable during the precipitation of Q1 cement. The sharp increase of pore water salinity with increasing burial depth (Figure 16B in Yuan, et al, 2015) and the strong fluid overpressure (Figure 11 in Cao et al, 2014) in the deep-water fan sandstone reservoirs have been reported to preclude any significant influx of meteoric water (Bjørlykke and Jahren, 2012; Yuan et al., 2015a). The distances of the location of the studied samples to the regional unconformity beneath the Ng formation are generally larger than 1500 m (4900 ft) (Table 1). Without widely development of faults connecting the unconformity and these sandstone reservoirs wrapped in the thick mudstones, feldspar leaching in these deep-water fan sandstones was unlikely related to meteoric freshwater (Bjørlykke and Jahren, 2012; Yuan et al, 2015a). Without a flux of meteoric fresh water into these sandstones, the decreasing trend of $\delta^{18}\text{O}_{(\text{water})}$ values in individual Q1 overgrowths (Figure 13A”) was probably induced by increasing temperatures during subsequent burial (Harwood et al., 2013). Because only aqueous inclusions were identified in Q1 quartz (Figure 10), oil was probably not imported into these sandstones during the Q1 cementation period.

Q2, as mentioned above, formed mainly from 115 °C (239 °F) to 130 °C (266 °F), and the $\delta^{18}\text{O}_{(\text{cement})}$ values decrease slightly or remain stable with the continuous growth of these overgrowths (Figure 13C”). Estimated $\delta^{18}\text{O}_{(\text{water})}$ values of the paleo-fluid from where Q2 precipitated range from +3‰ to +4.5‰ V-SMOW (Figure 15). The $\delta^{18}\text{O}_{(\text{cement})}$ values increase from Q1 to Q2 quartz, suggesting that the $\delta^{18}\text{O}_{(\text{water})}$ composition evolved to be heavier during the precipitation of Q2. Most fluid inclusions in Q2 quartz are oil inclusions and residual bitumen or oil was identified as being trapped between the Q2/Q1 boundary, indicating a primary oil-filling after Q1 quartz cementation. Color changes in the cold CL images (Figure 7) and trace element variations in Q1, Q2, and Q3 quartz (Figure 14) suggest that episodic oil emplacement imported some specific solutes (eg. Mn) into these sandstone reservoirs, forming the enrichment of Mn in Q2 quartz. The content of Mn in relevant mudstones and shales ranges mainly from 0.05% to 0.3% (Chen et al., 2016; Qian et al., 2009), which can be a potential solute to dissolve into the pore water and the petroleum in the source rocks. The Mn element can be moved from the source rocks to the reservoirs accompanying migration of hydrocarbon and relevant pore water during the hydrocarbon filling stage (Jian, 2009). As the volume of pore water in both reservoirs and shales is limited in the mesodiagenetic stage, the emplacement of large amount of fluids (include both hydrocarbons and saline pore water) from source rocks to reservoirs is likely to change the composition of the pore water in the sandstones significantly. The continuous enrichment of pore water in $\delta^{18}\text{O}$ during this period can be likely attributed to the on-going hydrocarbon emplacement and water-rock interactions in both sandstones and interbedded mudstones (Aplin and Warren, 1994; Marchand et al., 2002). The possible water-rock reactions at work include the illitization of kaolinite and illite/smectite mixed layer, and the recrystallization of carbonate minerals (Wilkinson et al., 1992).

5.4.2 Acids promoting feldspar dissolution

As temperature increase, acids are rendered unnecessary for feldspar decomposition during burial processes (Giles and De Boer, 1990; Taylor et al., 2010). The H^+ in a fluid, however, can be a significant catalyst for fast dissolution of silicate minerals (Kampman et al., 2009).

Carbonic acid in meteoric freshwater (Bjørlykke, 2014) has been suggested as a potential acid for mineral

leaching in deep-water sandstones. The petrographic textures (Figure 6), the high T_h values of the aqueous inclusions (Figure 11), and the calculated positive $\delta^{18}O_{(water)}$ values of paleo-fluids where quartz cements were formed (Figure 15) suggest that quartz cementation and simultaneous feldspar dissolution probably occurred in a geochemical system with limited volumes of diagenetic waters (Aplin and Warren, 1994); these waters are likely diagenetically modified connate water that has remained unaffected by meteoric freshwater (Girard et al., 2001; Harwood et al., 2013). Thus, carbonic acid in meteoric freshwater is unlikely to have promoted the extensive feldspar dissolution that was accompanied by quartz cementation in the sandstones we examined.

The leaching potential of organic acids and CO_2 originating from kerogen maturation in the source rocks to form secondary pores in sandstones have been debated for many years, and at issue is whether these acids will be consumed extensively in the source rocks themselves (Giles and Marshall, 1986; Taylor et al., 2010). With an average content of 5% TOC in the main mudstones and shales in the Shahejie Formation, and a high mud/sand ratio of 10:1 to 30:1 (Figure 3), the thermal evolution of organic matter in the source rocks can generate large quantities of CO_2 , organic acids, and hydrocarbons (Guo et al., 2010; Yuan et al., 2015b). The mudstones and shales in the Shengtuo area generally contain 5% to 45% carbonate minerals (Qian et al., 2009). If an extensive internal consumption of acids by these carbonate minerals occurred, the acids from kerogen maturation could not have been transported from the source rocks to the sandstone reservoirs effectively (Bjørlykke, 2014; Giles and Marshall, 1986; Taylor et al., 2010), and the organic-origin CO_2 -leaching and organic acid leaching hypotheses (Schmidt and McDonald, 1979; Surdam and Boese, 1984) cannot be used to explain the feldspar dissolution.

Carbonate minerals can be leached much faster than silicate minerals in an open geochemical system (Giles et al., 1986; Yuan et al., 2015b). Based on studies of petrography, isotope composition of CO_2 gas and carbonate cements, and numerical simulation of a CO_2 -feldspar-calcite interaction with constraints of pore water and CO_2 partial pressure, however, it has been proposed that feldspars were selectively dissolved in the presence of carbonate minerals in subsurface geochemical systems with a limited volume of pore water (Yuan et al., 2015b). The phenomena of selective dissolution of feldspars in the presence of carbonates are common in global sandstones and mudstones (Jia et al., 2016; Macquaker et al., 2014; Turchyn and DePaolo, 2011; Yuan et al., 2015b), and in the studied sandstones as well (Figure 6B, C). The calculated positive $\delta^{18}O_{(water)}$ data of the paleo-fluids (Figure 15) in this study suggests limited volumes of diagenetic water in the sandstones and mudstones we examined (Aplin and Warren, 1994). In such a geochemical system with a limited water volume, the suppression of pure carbonate dissolution likely occurred in mudstones and sandstones during the kerogen decarboxylation stage (Yuan et al., 2015b), which can be verified by the intact textures of the detrital carbonate grains and early carbonate cements in the sandstone reservoirs (Figure 6B, C). Recrystallization of the carbonate minerals may have occurred in the mudstones (Zhang et al., 2016), but an integrated recrystallization reaction did not consume acids.

Without extensive internal consumption of the acids produced by the kerogen maturation in the source rocks, the acids were likely transferred to the sandstones wrapped in the source rocks, and to selectively dissolve the feldspars and form the authigenic quartz and clays. The concentration of organic acids in the Bohai Bay Basin has a peak concentration of 2000-3000 ppm (0.32-0.48 oz/gal) at temperatures of 70-120 °C (158-248 °F), and

the concentration decreases from 2000 ppm to less than 500 ppm as temperature increases from 120 °C (248 °F) to 160 °C (320 °F) (Yuan et al., 2013). The tested CO₂ in the hydrocarbon-rich natural gas (Table 4) and the organic acids in the pore waters from the sandstone reservoirs from 2000 m (6560 ft) to 4000 m (13120 ft) (Yuan et al., 2013) all demonstrate that organic acids and organic-origin CO₂ probably have been transported from the source rocks to the sandstone reservoirs. These deep-water fan sandstones were trapped directly in the thick source rocks (Figure 3), and the transport of acids from such source rocks to the reservoirs also occurred easily. As discussed above, only aqueous inclusions were identified in Q1 quartz; further, gas bubbles were clearly present in these inclusions at room temperature (Figure 10). CO₂ was detected in the aqueous inclusion (Chen et al., 2010), indicating the generation of CO₂ and some organic acids from kerogen maturation in the source rocks before peak hydrocarbon generation. These acids were likely transported into the sandstones and promoted the feldspar leaching reactions, and the precipitation of Q1 quartz. Q2 quartz cementation occurred simultaneously or slightly postdating the main phase of oil filling. The complexation reactions between aluminum and carboxylic acids and phenols in the sandstone reservoirs after hydrocarbon emplacement likely reduced the Al³⁺ concentration in the pore water (Surdam et al., 1989), and led to the low concentration of aluminum in Q2 quartz. The CO₂ and organic acids dissolved in the oil were likely imported into the reservoirs accompanying the hydrocarbon migration. Further, thermal decarboxylation of aqueous n-alkanes in sandstone reservoirs can generate more CO₂ and organic acids to promote the leaching reaction of feldspars at higher temperatures (Seewald, 2003; Van Berk et al., 2013), as verified by the residual bitumen in the feldspar-hosted pores (Figure 6H, I) or trapped in the Q1/Q2 quartz boundary (Figure 10). The organic acids, hydrocarbon, CO₂, and the high CO₂ partial pressure (Table 4) in the present reservoirs indicate that the CO₂ and organic acids from the thermal evolution of organic matter (kerogen in source rocks and hydrocarbon in reservoirs) probably promoted the feldspar leaching reactions accompanying the precipitation of Q2 quartz. For Q3 quartz cementation at high temperature in deeply buried reservoirs, most organic acids likely were decomposed to form CO₂ (Seewald, 2003; Surdam et al., 1989). The CO₂ partial pressure in such deeply buried reservoirs can reach up to more than 30 bar (3MPa) (Table 4), which would have promoted feldspar leaching at high temperatures. At this stage, a release of Al³⁺ from complexes due to decarboxylation of organic acids likely increased the Al³⁺ concentration in the pore water and led to the high concentration of aluminum in Q3 quartz (Figure 14). The development of Q2 and Q3 quartz in the sandstones we examined suggests that quartz cementation did not cease after hydrocarbon emplacement. Further, the diagenetic reactions likely proceeded from water-rock interactions to hydrocarbon-water-rock interactions (Seewald, 2003; Van Berk et al., 2013).

In short, the answer to feldspar leaching and relevant water-rock interactions in the Shengtuo deep-water fan sandstones is not found flowing in the meteoric freshwater, but rather in understanding the evolution of the pore water at work during the mesodiagenetic stage.

6 Conclusions

Leached feldspars, quartz cements, and authigenic clays are present in the Shengtuo feldspar-rich porous sandstones in Dongying sag, East China. The internal feldspar dissolution provided the main source of silica for the quartz cements in the sandstones. The homogenization temperature of aqueous inclusions in quartz

overgrowths and $\delta^{18}\text{O}$ compositions of quartz overgrowths suggest that the quartz cementation and simultaneous extensive feldspar dissolution occurred in geochemical systems with high threshold temperature ($>95\text{-}100\text{ }^\circ\text{C}$ ($203\text{-}212\text{ }^\circ\text{F}$)) and in the diagenetic pore water with positive oxygen compositions.

Moreover, this study suggests that if diagenetic mineral assemblages in sandstones can be identified, it is possible to investigate the origin of the leaching reactions using geochemical information from relevant authigenic minerals. In the Shengtuo sandstones, the feldspar leaching reaction is irrelevant to meteoric freshwater. As carbonate mineral dissolution is suppressed in geochemical systems with a limited volume of water, the acids from the thermal evolution of organic matter likely promoted the subsurface dissolution of large amounts of feldspars in the deep-water fan feldspar-rich sandstones we investigated. The chemical diagenetic reactions can continue after oil filling, and likely proceeded from water-rock interactions to hydrocarbon-water-rock interactions.

References:

- Alekseyev, V. A., L. S. Medvedeva, N. I. Prisyagina, S. S. Meshalkin, and A. I. Balabin, 1997, Change in the dissolution rates of alkali feldspars as a result of secondary mineral precipitation and approach to equilibrium: *Geochimica et Cosmochimica Acta*, v. 61, no. 6, p. 1125-1142.
- Aplin, A. C., and E. A. Warren, 1994, Oxygen isotopic indications of the mechanisms of silica transport and quartz cementation in deeply buried sandstones: *Geology*, v. 22, no. 9, p. 847-850.
- Barclay, S. A., and R. H. Worden, 2000, Geochemical modelling of diagenetic reactions in a sub-arkosic sandstone: *Clay Minerals*, v. 35, no. 1, p. 57-67.
- Bjørlykke, K., 2011, Open-system chemical behavior of Wilcox Group mudstones. How is large scale mass transfer at great burial depth in sedimentary basins possible? A discussion: *Marine and Petroleum Geology*, v. 28, no. 7, p. 1381-1382.
- Bjørlykke, K., 2014, Relationships between depositional environments, burial history and rock properties. Some principal aspects of diagenetic process in sedimentary basins: *Sedimentary Geology*, v. 301, p. 1-14.
- Bjørlykke, K., and J. Jahren, 2012, Open or closed geochemical systems during diagenesis in sedimentary basins: Constraints on mass transfer during diagenesis and the prediction of porosity in sandstone and carbonate reservoirs: *AAPG Bulletin*, v. 96, no. 12, p. 2193-2214.
- Cao, Y. C., G. H. Yuan, X. Y. Li, Y. Z. Wang, K. L. Xi, X. M. Wang, Z. Z. Jia, and T. Yang, 2014, Characteristics and origin of abnormally high porosity zones in buried Paleogene clastic reservoirs in the Shengtuo area, Dongying Sag, East China, v. 11, no. 3, p. 346-362.
- Chen, Y., C. Lin, S. Zhang, and G. Song, 2010, Study on fluid inclusions in deep natural gas reservoirs in Minfeng subsag, Dongying Sag: *Acta Sedimentologica Sinica*, v. 28, no. 3, p. 620-625.
- Chen, Z., W. Huang, Q. Liu, L. Zhang, and S. Zhang, 2016, Geochemical characteristics of the Paleogene shales in the Dongying depression, eastern China: *Marine & Petroleum Geology*, v. 73, p. 249-270.
- Dutton, S. P., and R. G. Loucks, 2010, Diagenetic controls on evolution of porosity and permeability in lower Tertiary Wilcox sandstones from shallow to ultradeep (200 - 6700m) burial, Gulf of Mexico Basin, U.S.A.: *Marine and Petroleum Geology*, v. 27, no. 1, p. 69-81.
- Fayek, M., T. M. Harrison, M. Grove, K. D. Mckeegan, C. D. Coath, and J. R. Boles, 2001, In situ Stable Isotopic Evidence for Protracted and Complex Carbonate Cementation in a Petroleum Reservoir, North Coles Levee, San Joaquin Basin, California, U.S.A: *Journal of Sedimentary Research*, v. 71, no. 3, p. 444-458.
- French, M. W., 2012, Quartz growth: understanding porosity-preserving microcrystalline quartz through EBSD,

TEM, and NanoSIMS examination of low temperature silica: Doctoral dissertation, University of Liverpool.

Fu, Q., P. Lu, H. Konishi, R. Dilmore, H. Xu, W. E. Seyfried, and C. Zhu, 2009, Coupled alkali-feldspar dissolution and secondary mineral precipitation in batch systems: 1. New experiments at 200 °C and 300 bars: *Chemical Geology*, v. 258, no. 3, p. 125-135.

Giles, M. R., and J. D. Marshall, 1986, Constraints on the development of secondary porosity in the subsurface: re-evaluation of processes: *Marine and Petroleum Geology*, v. 3, no. 3, p. 243-255.

Giles, M. R., and R. B. De Boer, 1990, Origin and significance of redistributional secondary porosity: *Marine and Petroleum Geology*, v. 7, no. 4, p. 378-397.

Girard, J., I. A. Munz, H. Johansen, S. Hill, and A. Canham, 2001, Conditions and timing of quartz cementation in Brent reservoirs, Hild Field, North Sea: constraints from fluid inclusions and SIMS oxygen isotope microanalysis: *Chemical Geology*, v. 176, no. 1, p. 73-92.

Glasmann, J. R., 1992, The fate of feldspar in Brent Group reservoirs, North Sea: A regional synthesis of diagenesis in shallow, intermediate, and deep burial environments: Geological Society, London, Special Publications, v. 61, no. 1, p. 329-350.

Guo, X., K. Liu, S. He, G. Song, Y. Wang, X. Hao, and B. Wang, 2012, Petroleum generation and charge history of the northern Dongying Depression, Bohai Bay Basin, China: Insight from integrated fluid inclusion analysis and basin modelling: *Marine and Petroleum Geology*, v. 32, no.1, p. 21-35.

Guo, X., S. He, K. Liu, G. Song, X. Wang, and Z. Shi, 2010, Oil generation as the dominant overpressure mechanism in the Cenozoic Dongying depression, Bohai Bay Basin, China: *AAPG Bulletin*, v. 94, no.12, p. 1859-1881.

Harwood, J., A. C. Aplin, C. I. Fialips, J. E. Iliffe, R. Kozdon, T. Ushikubo, and J. W. Valley, 2013, Quartz cementation history of sandstones revealed by high-resolution SIMS oxygen isotope analysis: *Journal of Sedimentary Research*, v. 83, no. 7, p. 522-530.

Higgs, K. E., H. Zwingmann, A. G. Reyes, and R. H. Funnell, 2007, Diagenesis, porosity evolution, and petroleum emplacement in tight gas reservoirs, Taranaki Basin, New Zealand: *Journal of Sedimentary Research*, v. 77, no. 12, p. 1003-1025.

Hutcheon, I., M. Shevalier, and H. J. Abercrombie, 1993, pH buffering by metastable mineral-fluid equilibria and evolution of carbon dioxide fugacity during burial diagenesis: *Geochimica et Cosmochimica Acta*, v. 57, no. 5, p. 1017-1027.

Jia, Z. Z., C. Y. Lin, L. H. Ren, and C. M. Dong, 2016, Selective dissolution of eodiagenesis cements and its impact on the quality evolution of reservoirs in the Xing'anling Group, Suderte Oil Field, Hailar Basin, China: *Petroleum Science*, v. 13, no. 3, p. 1-16.

Jian, C., 2009, Manganese in reservoir calcite cement and its implication for tracing oil migration in Junggar Basin: *Acta Petrolei Sinica*, v. 30, no. 5, p. 705-710.

Kampman, N., M. Bickle, J. Becker, N. Assayag, and H. Chapman, 2009, Feldspar dissolution kinetics and Gibbs free energy dependence in a CO₂-enriched groundwater system, Green River, Utah: *Earth and Planetary Science Letters*, v. 284, no. 3, p. 473-488.

Kelly, J. L., B. Fu, N. T. Kita, and J. W. Valley, 2007, Optically continuous silcrete quartz cements of the St. Peter Sandstone: High precision oxygen isotope analysis by ion microprobe: *Geochimica et Cosmochimica Acta*, v. 71, no. 15, p. 3812-3832.

Lai J, Wang G., Chai Y., Xin Y., Wu Q., Zhang X., and Sun Y, 2017. Deep burial diagenesis and reservoir quality evolution of high-temperature, high-pressure sandstones: Examples from Lower Cretaceous Bashijiqike Formation in Keshen area, Kuqa depression, Tarim basin of China. *AAPG Bulletin*, v. 101, no. 3, doi:10.1306/08231614008.

Lehmann, K., T. Pettke, and K. Ramseier, 2011, Significance of trace elements in syntaxial quartz cement, Haushi Group sandstones, Sultanate of Oman: *Chemical Geology*, v. 280, no. 1, p. 47-57.

- Li, X., G. Tang, B. Gong, Y. Yang, K. Hou, Z. Hu, Q. Li, Y. Liu, and W. Li, 2013, Qinghu zircon: A working reference for microbeam analysis of U-Pb age and Hf and O isotopes: *Chinese Science Bulletin*, v. 58, no. 36, p. 4647-4654.
- Li, X., Z. Li, B. He, W. Li, Q. Li, Y. Gao, and X. Wang, 2012, The Early Permian active continental margin and crustal growth of the Cathaysia Block: In situ U - Pb, Lu - Hf and O isotope analyses of detrital zircons: *Chemical Geology*, v. 328, p. 195-207.
- Lundegard, P. D., L. S. Land, and W. E. Galloway, 1984, Problem of secondary porosity: Frio Formation (Oligocene), Texas Gulf Coast: *Geology*, v. 12, no. 7, p. 399-402.
- Macquaker, J. H. S., K. G. Taylor, M. Keller, and D. Polya, 2014, Compositional controls on early diagenetic pathways in fine-grained sedimentary rocks: Implications for predicting unconventional reservoir attributes of mudstones: *AAPG Bulletin*, v. 98, no. 3, p. 587-603.
- Marchand, A. M. E., C. I. Macaulay, R. S. Haszeldine, and A. E. Fallick, 2002, Pore water evolution in oilfield sandstones: constraints from oxygen isotope microanalyses of quartz cement: *Chemical Geology*, v. 191, no. 4, p. 285-304.
- Mcbride, E. F., 1989, Quartz cement in sandstones: a review: *Earth Science Reviews*, v. 26, no. 1-3, p. 69-112.
- Méheut, M., M. Lazzeri, E. Balan, and F. Mauri, 2007, Equilibrium isotopic fractionation in the kaolinite, quartz, water system: Prediction from first-principles density-functional theory: *Geochimica et Cosmochimica Acta*, v. 71, no. 13, p. 3170-3181.
- Molenaar, N., M. Felder, K. Bär, and A. E. Götz, 2015, What classic greywacke (litharenite) can reveal about feldspar diagenesis: An example from Permian Rotliegend sandstone in Hessen, Germany: *Sedimentary Geology*, v. 326, p. 79-93.
- Pollington, A. D., R. Kozdon, and J. W. Valley, 2011, Evolution of quartz cementation during burial of the Cambrian Mount Simon Sandstone, Illinois Basin: In situ microanalysis of $\delta^{18}\text{O}$: *Geology*, v. 39, no. 12, p. 1119-1122.
- Qian, J., C. Lu, X. Zhang, L. Zhang, and Q. Liu, 2009, Spatial paleosalinity distribution and element geochemistry of argillaceous source rocks in the upper part of 4th Member of Tertiary Shahejie Formation in Dongying Sag: *Acta Petrologica Et Mineralogica*, v. 28, no. 2, p. 161-168.
- Robinson, A., and J. Gluyas, 1992, Duration of quartz cementation in sandstones, North Sea and Haltenbanken Basins: *Marine & Petroleum Geology*, v. 9, no.3, p. 324-327.
- Saigal, G. C., and K. Bjørlykke, 1987, Carbonate cements in clastic reservoir rocks from offshore Norway--relationships between isotopic composition, textural development and burial depth: *Geological Society, London, Special Publications*, v. 36, no. 1, p. 313-324.
- Schmidt, V., and D. A. McDonald, 1979, The role of secondary porosity in the course of sandstone diagenesis: *SPEM Special Publication*, No.26, p. 175-207.
- Seewald, J. S., 2003, Organic-inorganic interactions in petroleum-producing sedimentary basins: *Nature*, v. 426, no. 6964, p. 327-33.
- Smith, J. T., and S. N. Ehrenberg, 1989, Correlation of carbon dioxide abundance with temperature in clastic hydrocarbon reservoirs: relationship to inorganic chemical equilibrium: *Marine and Petroleum Geology*, v. 6, no.2, p. 129-135.
- Stoessell, R. K., 1987, Mass transport in sandstones around dissolving plagioclase grains: *Geology*, v. 15, no. 4, p. 295-298.
- Surdam, R. C., L. J. Crossey, E. S. Hagen, and H. P. Heasler, 1989, Organic-inorganic interactions and sandstone diagenesis: *AAPG Bulletin*, v. 73, no.1, p. 1-23.
- Surdam, R. C., and S. W. Boese, 1984, The chemistry of secondary porosity: *AAPG Memoir*, 1984, v. 37, no. 2, p. 183-200.
- Taylor, T. R., M. R. Giles, L. A. Hathon, T. N. Diggs, N. R. Braunsdorf, G. V. Birbiglia, M. G. Kittridge, C. I.

Macaulay, and I. S. Espejo, 2010, Sandstone diagenesis and reservoir quality prediction: Models, myths, and reality: AAPG Bulletin, v. 94, no. 8, p. 1093-1132.

Thyne, G., 2001, A model for diagenetic mass transfer between adjacent sandstone and shale: Marine and petroleum geology, v. 18, no. 6, p. 743-755.

Thyne, G., B. P. Boudreau, M. Ramm, and R. E. Midtbo, 2001, Simulation of potassium feldspar dissolution and illitization in the Statfjord Formation, North Sea: AAPG bulletin, v. 85, no. 4, p. 621-637.

Turchyn, A. V., and D. J. DePaolo, 2011, Calcium isotope evidence for suppression of carbonate dissolution in carbonate-bearing organic-rich sediments: Geochimica et Cosmochimica Acta, v. 75, no. 22, p. 7081-7098.

Van Berk, W., H. Schulz, and Y. Fu, 2013, Controls on CO₂ fate and behavior in the Gullfaks oil field (Norway): How hydrogeochemical modeling can help decipher organic-inorganic interactions: AAPG Bulletin, v. 97, no.12, p. 2233-2255.

Van der Plas, L., and A. C. Tobi, 1965, A chart for judging the reliability of point counting results: American Journal of Science, v. 263, no. 1, p. 87-90.

Walderhaug, O., 1996, Kinetic modeling of quartz cementation and porosity loss in deeply buried sandstone reservoirs: AAPG Bull, v. 80, no. 5, p. 731-745.

Walderhaug, O., 2000, Modeling quartz cementation and porosity in Middle Jurassic Brent Group sandstones of the Kvitebjørn Field, Northern North Sea I: AAPG Bull, v. 84, no. 9, p. 1325-1339.

Wang, Y., Y. C. Cao, K. L. Xi, G. Song, and H. M. Liu, 2013, A recovery method for porosity evolution of clastic reservoirs with geological time: a case study from the upper submember of Es4 in the Dongying depression, Jiayang subsasin (In Chinese with English abstract): Acta Petrol Sin, v.34, no. 6, p. 1100-1111.

Wilkinson, M., K. L. Milliken, and R. S. Haszeldine, 2001, Systematic destruction of K-feldspar in deeply buried rift and passive margin sandstones: Journal of the Geological Society, v. 158, no. 4, p. 675-683.

Wilkinson, M., S. F. Crowley, and J. D. Marshall, 1992, Model for the evolution of oxygen isotope ratios in the pore fluids of mudrocks during burial: Marine & Petroleum Geology, v. 9, no. 1, p. 98-105.

Williams, L. B., R. L. Hervig, and K. Bj Rlykke, 1997, New evidence for the origin of quartz cements in hydrocarbon reservoirs revealed by oxygen isotope microanalyses: Geochimica et Cosmochimica Acta, v. 61, no.12, p. 2529-2538.

Worden, R. H., and S. A. Barclay, 2000, Internally-sourced quartz cement due to externally-derived CO₂ in sub-arkosic sandstones, North Sea: Journal of Geochemical Exploration, v. 69, p. 645-649.

Worden, R. H., and S. Morad, 2000, Quartz cementation in oil field sandstones: a review of the key controversies. Quartz cementation in sandstones. International Association of Sedimentologists Special publication, 29: 1-20.

Yuan, G. H., Y. C. Cao, K. L. XI, Y. Z. Wang, X. Y. Li, and T. Yang, 2013, Feldspar dissolution and its impact on physical properties of Paleogene clastic reservoirs in the northern slope zone of the Dongying sag: Acta Petrolei Sinica, v. 34, no. 5, p. 853-866. (In Chinese with English abstract).

Yuan, G., Y. Cao, J. Gluyas, X. Li, K. Xi, Y. Wang, Z. Jia, P. Sun, and N. H. Oxtoby, 2015a, Feldspar dissolution, authigenic clays, and quartz cements in open and closed sandstone geochemical systems during diagenesis: Typical examples from two sags in Bohai Bay Basin, East China: AAPG Bulletin, v. 99, no. 11, p. 2121-2154.

Yuan, G., Y. Cao, T. Yang, Y. Wang, X. Li, K. Xi, and Z. Jia, 2013, Porosity enhancement potential through mineral dissolution by organic acids in the diagenetic process of clastic reservoir: Earth Science Frontiers, v. 20, no. 5, p. 207-219.

Yuan, G., Y. Cao, Z. Jia, J. Gluyas, T. Yang, Y. Wang, and K. Xi, 2015b, Selective dissolution of feldspars in the presence of carbonates: The way to generate secondary pores in buried sandstones by organic CO₂: Marine and Petroleum Geology, v. 60, p. 105-119.

Yuan, G., J. Gluyas, Y. Cao, N. H. Oxtoby, Z. Jia, Y. Wang, K. Xi, and X. Li, 2015c, Diagenesis and reservoir

quality evolution of the Eocene sandstones in the northern Dongying Sag, Bohai Bay Basin, East China: *Marine and Petroleum Geology*, v. 62, p. 77-89.

Yuan, J., and Q. Z. Wang, 2001, Distribution and generation of deep reservoir secondary pores, Paleogene, Dongying Sag: *Journal Petrol*, v. 21, no. 1, p. 43-47. (In Chinese with English abstract).

Zhang, J., Z. Jiang, X. Jiang, S. Wang, C. Liang, and M. Wu, 2016, Oil generation induces sparry calcite formation in lacustrine mudrock, Eocene of east China: *Marine & Petroleum Geology*, v. 71, p. 344-359.

Zhang, Q., X. Zhu, R. J. Steel, and D. Zhong, 2014, Variation and mechanisms of clastic reservoir quality in the Paleogene Shahejie Formation of the Dongying Sag, Bohai Bay Basin, China: *Petroleum Science*, v. 11, no. 2, p. 200-210.

Zhu, C., A. E. Blum, and D. R. Veblen, 2004, Feldspar dissolution rates and clay precipitation in the Navajo aquifer at Black Mesa, Arizona, USA: *Water-Rock Interaction*, p. 895-899.

Zhu, C., P. Lu, Z. Zheng, and J. Ganor, 2010, Coupled alkali feldspar dissolution and secondary mineral precipitation in batch systems: 4. Numerical modeling of kinetic reaction paths: *Geochimica et Cosmochimica Acta*, v. 74, no. 14, p. 3963-3983.

Zhu, C., and P. Lu, 2009, Alkali feldspar dissolution and secondary mineral precipitation in batch systems: 3. Saturation states of product minerals and reaction paths: *Geochimica et Cosmochimica Acta*, v. 73, no. 11, p. 3171-3200.

Preliminary
Version

Figure 1 Location map and cross section of the Shengtuo area, Dongying sag, East China. Modified from Yuan et al (2015a) and used with permission of AAPG. Symbols represent locations of samples with different analysis.

Figure 2 Generalized Cenozoic-Quaternary stratigraphy in the Shengtuo area, Dongying sag showing tectonic and sedimentary evolution stages and the major petroleum system elements (Yuan et al., 2015a) (used with permission of AAPG).

Figure 3 (A) Distribution map of the sublacustrine fans in the Es₄¹ sub-member in the Shengtuo area, Dongying sag (modified from Cao et al, 2014) (used with permission of Springer). (B, C) Columns showing the depositional characteristics of the sublacustrine fans and deep lake facies in the Shengtuo area, Dongying sag. SP: spontaneous potential logging curve; RT: resistivity logging curve.

Figure 4 Secondary ion mass spectrometry (SIMS) oxygen isotope analyses of the international quartz standard NBS-28 performed in the course of the study.

Figure 5 General diagenetic sequence of the studied sandstones in the Shengruo area, Dongying sag (after Yuan et al, 2015b) (used with permission of Elsevier).

Figure 6 Photomicrographs of leached feldspars, relevant authigenic clays, and residual bitumen in feldspar-hosted pores in sandstones. PPL-plane polarized light view, XL-cross polarized light view, UV-UV light view, SEM-scanning electron microscopy view. (A) tight sandstone with large amount of carbonate cements, feldspars were not leached; (B, C) intact detrital carbonate grains and early grain-coating carbonate cements where feldspar was dissolved extensively (after Yuan et al, 2015b) (used with permission of Elsevier); (D) extensive leached feldspars with precipitation of secondary minerals (after Yuan et al, 2015c) (used with permission of Elsevier); (E, F, G) secondary pores after feldspar grains preserve the original outlines of former grains, indicating a weak compaction accompanying the leaching reactions; (H, I) residual bitumen in feldspar-hosted pores, indicating oil cracking during deep burial; (J) authigenic kaolinite and quartz overgrowths in thin sections; (K) authigenic fibrous illite in formed accompanying feldspar dissolution (after Cao et al, 2014) (used with permission of Springer); (L) mixture of authigenic kaolinite and quartz crystals, indicating simultaneous precipitation of these cements. Q-quartz grain, F-feldspar grain, Ca-calcite cement, DC-detrital calcite grain, FD-feldspar-hosted pores, Cc-carbonate cement, K-kaolinite, Qo-quartz overgrowths, I-illite, Bi-bitumen.

Figure 7 Photomicrographs of quartz overgrowths identified with optical and CL microscopy. PPL-plane polarized light view, CL-cathodoluminescence view. (A, A') Q1 quartz overgrowths; (B, B') Q2 quartz overgrowths formed directly on detrital quartz grains; (C, C') Q1 and Q2 quartz overgrowths, Q2 quartz was formed on Q1 quartz; (D, D') Q1, Q2 and Q3 quartz overgrowths on one detrital quartz grain. Q-quartz grain, F-feldspar grain, Q1-the first phase of quartz overgrowths, Q2- the second phase of quartz overgrowths, Q3-the third phase of quartz overgrowths.

Figure 8 Scanning electron microscope (SEM) images of authigenic clays, quartz cements, and feldspar dissolution in the sandstone samples. (A) leached feldspars, authigenic kaolinite and quartz cements; (B) mixture of authigenic kaolinite and quartz cements; (C) authigenic kaolinite; (D) mixture of authigenic kaolinite and quartz crystals (after Yuan et al, 2015a) (used with permission of AAPG); (E) authigenic illite on ankerite cement; (F) fibrous illite. Qc: quartz cement, LF: leached feldspar, K: kaolinite, Qc: quartz crystal; An: ankerite, I: illite.

Figure 9 Relationships between the amount of feldspar-hosted pores and secondary minerals in the thin sections.

Figure 10 Petrography of fluid inclusions trapped in quartz overgrowths, detrital-authigenic quartz boundary or healed microfractures. PPL-plane polarized light view, UV-UV light view. (A, B, C, D) aqueous inclusion in Q1 quartz and oil inclusions in Q2 quartz, oil or bitumen trapped in the Q1/Q2 boundary; (E, F) aqueous inclusion in Q1 quartz, Q1/detrital quartz boundary and healed microfracture; (G, H) aqueous inclusion in Q1/detrital quartz boundary and oil inclusion in Q2 quartz. Q-quartz grain, Q1-the first phase of quartz overgrowths, Q2- the second phase of quartz overgrowths, AI-aqueous fluid inclusion, Oi-oil fluid inclusion.

Figure 11 Histograms of the homogenization temperature (T_h) for aqueous inclusions in different phases of quartz overgrowths in the Shengtuo sandstones.

Figure 12 Histograms showing the distribution of $\delta^{18}O_{\text{‰v-SMOW}}$ values of detrital quartz grains and authigenic quartz overgrowths in four sandstone samples.

Figure 13 Evolution of $\delta^{18}\text{O}(\text{cement})$ compositions in individual quartz overgrowths. CL-cathodoluminescence view, RL-reflected light view.

(A, A', A'') decrease evolution trend of $\delta^{18}\text{O}\text{‰}(\text{cement})$ in Q1 quartz; (B, B, B'') decrease evolution trend of $\delta^{18}\text{O}\text{‰}(\text{cement})$ in Q1 quartz; (C, C', C'') evolution of $\delta^{18}\text{O}\text{‰}(\text{cement})$ from Q1 quartz to Q2 quartz; (D, D', D'') evolution of $\delta^{18}\text{O}\text{‰}(\text{cement})$ from Q1 quartz to Q2 quartz and Q3 quartz.

Figure 14 Plane-polarized light (PPL) and cathodoluminescence (CL) views showing analysis locations and wavelength dispersive spectroscopy (WDS) analysis of the content of trace elements along a profile from the detrital quartz grain to the quartz overgrowths (including Q1, Q2 and Q3). Q1 and Q3 quartz contain more aluminium than Q2 quartz, while Q2 quartz has more manganese than Q1 and Q2 quartz.

Figure 15 Cross plot of $\delta^{18}\text{O}$ (quartz cement) in equilibrium with water ($\delta^{18}\text{O}(\text{water}) = -3\text{‰}, -2\text{‰}, -1\text{‰}, 0\text{‰}, +1\text{‰}, +2\text{‰}, +3\text{‰}, +4\text{‰}$) as a function of temperature (Méheut, 2007).

Preliminary
Version

Table 1 Thin section compositions from optical point counting and quantitative image analysis. QC: quartz overgrowths. 0.2^K: the content of kaolinite in the thin section; 0.2^I: the content of illite in the thin section; “?”: not applicable; “-”: the content of the authigenic illite in the thin section was not obtained because the distribution of the illite was too dispersive.

Borehole	TVD, m /ft	Distance to unconformity, m/ft	Quartz, %	Feldspar, %	Rock fragment, %	Detrital clay, %	Carbonate cement, %	Authigenic clay, % (without calibration of micropores)	QC, %	Feldspar-hosted pores, %	Expected kaolinite from leached feldspars, %	Expected quartz from leached feldspars, %	Core porosity, %	Lithofacies
Tuo 73	3368.40/ 11051.18	1955/6414	23	45	32	0.2	25	Scarce (<0.01)	Scarce (<0.01)	Scarce (<0.01)	/	/	3.5	fine- to medium-grained sandstone
Tuo 73	3371.25/ 11060.53	1958/6423	25	47	28	<0.1	8	0.1 ^I	0.05	0.2	0.09	0.08	10.2	fine- to medium-grained sandstone
Tuo 76	2942.02/ 9652.30	1504/4934	40	44	16	1	0.5	0.2 ^K	0.1	0.2	0.09	0.08	22.3	medium-grained sandstone
Tuo 76	3340.91/ 0960.96	1902/6240	27	45	28	0.5	30	Scarce (<0.01)	Scarce (<0.01)	Scarce (<0.01)	/	/	1.2	fine- to medium-grained sandstone
Tuo 76	3457.78/ 11344.42	2019/6860	39	34	27	2	8	-	0.4	1.0	0.47	0.42	12.9	medium- to coarse-grained sandstone
Tuo168	3098.25/ 10164.86	1595/5232.94	24	50	26	0.2	3	0.2 ^I	0.1	0.3	0.14	0.12	15.6	medium-grained sandstone
Tuo 168	3100.20/ 10204.07	1597/5239	27	46	27	0.2	20	0.1 ^I	0.1	0.3	0.14	0.12	7.9	medium-grained sandstone
Tuo 168	3110.10/ 10203.74	1607/5272	23	48	29	0.3	7	0.4 ^I	0.2	0.5	0.24	0.21	16.2	medium-grained sandstone
Tuo 712	3167.32/ 10391.47	1747/5731	31	45	24	0.5	6	1.6 ^K	0.4	1.2	0.57	0.50	10.3	medium- to coarse-grained sandstone
Tuo 713	3029.60/ 9939.63	1579/5180	44	29	27	0.1	11	1.4 ^K	0.5	1.4	0.66	0.58	11.2	fine-grained conglomerate
Tuo 713	3032.45/ 9948.98	1582/5190	30	47	23	0.1	12	1.2 ^K	0.3	0.7	0.33	0.29	11.7	fine-grained conglomerate
Tuo 714	2780.40/ 912.04	1295/4248	27	63	10	0.3	13	1.9 ^K	0.6	1.3	0.61	0.54	4.7	medium- to coarse-grained sandstone
Tuo 714	2841.30/ 9321.85	1353/4439	41	46	13	0.1	5	2.9 ^K	0.7	2.5	1.18	1.04	19.9	medium- to coarse-grained sandstone
Tuo 720	3535.00/ 11597.77	2161/7090	36	48	16	0.1	4	-	0.9	2.3	1.09	0.96	19.0	fine-grained conglomerate
Tuo 720	3536.05/ 11601.21	2162/7093	25	43	32	0.1	7	-	0.2	0.5	0.24	0.21	13.1	fine-grained conglomerate
Tuo 720	3671.10/ 12044.29	2297/7536	30	45	25	0.1	3	-	0.8	2.3	1.09	0.96	14.2	fine-grained conglomerate
Tuo 741	2941.25/ 9649.77	1516/4973	60	31	9	0.1	3	2.4 ^K	0.5	2.2	1.04	0.92	19.2	fine- grained sandstone
Tuo 741	2961.75/ 9717	1536/5039	50	36	14	0.1	1	2.7 ^K	0.7	2.2	1.04	0.92	22.3	fine- grained sandstone
Tuo 741	2972.75/ 9573.11	1547/5075	51	15	34	0.1	28	Scarce (<0.01)	Scarce (<0.01)	Scarce (<0.01)	/	/	2.4	fine- grained sandstone

Table 2 Size, shape and homogenization temperature of aqueous fluid inclusions in the quartz overgrowths in the Shengtuo sandstones

Well	Core depth / Temperature	Inclusion size (um)		Inclusion location	T _h (°C/°F)
		Long	Short		
Tuo 714	2843.00 m (9327.42ft) / 119 °C (246 °F)	6	3	O1/Grain boundary	113.7/236.7
		5	4	O1 quartz	109.5/229.1
		5	5	O1 quartz	113.7/236.7
		4	1	Q1/Grain boundary	110.8/231.4
		5	4	O1 quartz	111.3/232.3
		6	1	O1 quartz	115.1/239.2
		6	2	O1 quartz	111.8/233.2
Tuo720	3535.00 m (11597.76 ft) / 138 (280 °F)	5	4	O1 quartz/Grain boundary	108.7/227.66
		6	3	O1 quartz	114.5/238.1
		7	5	O1 quartz/Grain boundary	115.5/239.9
		6	5	O1 quartz	113.3/235.9
		8	7	Q2 quartz	122.2/259.96
		5	5	O1 quartz/Grain boundary	113.6/236.5
		10	10	O1 quartz	114.5/238.1
		6	3	O1 quartz	114.7/238.4
		8	6	Q2 quartz	117.2/242.9
		4	3	Q3 quartz/Grain boundary ?	137.7/279.8
		3	2	O1 quartz/Grain boundary	102.0/215.6
		5	4	O1 quartz	106.0/222.8
		4	3	O1 quartz	106.5/223.7
		3	2	O1 quartz	104.2/219.5
		3	2	O2 quartz	119.9/247.8
		4	3	O1 quartz	106.6/223.9
		13	4	Q2 quartz	126.6/259.9
		6	3	Q2 quartz	123.2/253.7
		3	2	O1 quartz	108.2/226.8
		3	2	O2 quartz	122.9/253.2
3	3	Q3 quartz ?	134.5/274.1		
3	2	Q3 quartz ?	135.4/275.7		
Tuo76	3465.25 m (11368.93 ft) / 136 (277 °F)	5	3	O1 quartz	113.7/236.6
		3	2	O1 quartz	107.0/224.6
		4	3	O1 quartz/Grain boundary	114.0/237.2
Tuo168	3110.10m (10203.74) / 126 (259 °F)	6	4	O1 quartz	104.2/219.2
		5	4	O1 quartz	102.1/215.8
		8	4	O1 quartz/Grain boundary	113.2/235.7
		4	3	Q2 quartz	125.6/258.08
		5	4	Q2 quartz	123.6/254.48
		4	3	Q2 quartz	119.8/247.64
		5	2	O1 quartz/Grain boundary	108.4/227.12
		5	4	O1 quartz	106.7/224.1
		4	2	O1 quartz Grain boundary	101.7/215.1

Table 3 Trace element compositions of a quartz overgrowths in the Shengtuo sandstones (Figure 14). n.d.: not detected.

Point	Trace elements in detrital quartz grain and quartz overgrowths, mass %									Quartz phases
	Na ₂ O	MgO	Al ₂ O ₃	K ₂ O	CaO	TiO ₂	FeO	MnO	Cr ₂ O ₃	
1	0.009	0.021	0.156	0.001	0.044	n.d.	0.017	0.012	0.017	Q3
2	n.d.	n.d.	0.086	n.d.	0.044	0.004	0.027	n.d.	n.d.	Q2
3	0.028	n.d.	0.025	0.025	0.027	n.d.	0.012	0.01	0.003	Q2
4	0.017	0.018	n.d.	0.006	0.036	0.007	0.024	0.026	n.d.	Q2
5	0.028	0.014	0.046	0.002	0.010	0.022	n.d.	n.d.	n.d.	Q1
6	n.d.	n.d.	0.108	0.017	0.032	n.d.	0.027	n.d.	n.d.	Q1
7	0.013	n.d.	0.020	n.d.	0.008	0.002	0.012	n.d.	n.d.	Q
8	n.d.	0.003	n.d.	n.d.	n.d.	n.d.	0.021	0.023	n.d.	Q
9	n.d.	0.013	0.156	0.027	0.019	n.d.	0.035	0.005	n.d.	Q1
10	0.052	0.007	0.033	0.022	0.016	n.d.	n.d.	0.016	n.d.	Q2
11	n.d.	0.014	0.17	0.005	n.d.	n.d.	0.013	n.d.	n.d.	Q3

Table 4 Natural gas compositions, tested fluid pressure and CO₂ partial pressure (pCO₂) in the Shengtuo sandstone reservoirs.

Wells	Depth (m/ft)	Strata	Fluid pressure (Mpa/bar)	Natural gas composition, mole%									pCO ₂ (bar/MPa)
				CH ₄	C ₂ H ₆	C ₃ H ₈	C ₄ H ₁₀	C ₃ H ₁₂	C _n H _{2n+2} , n>6	N ₂	H ₂ S	CO ₂	
Tuo133	3043-3128/ 9985-10262	ES ₄ ¹	31.19/311.9	45.80	11.77	16.88	12.00	0	5.00	1.99	0	5.66	17.6/1.76
Tuo160	2621-2663/ 8599-8737	ES ₃ ³	27.05/270.5	81.96	2.65	5.07	3.54	0	1.59	0.55	0	4.65	12.6/1.26
Tuo166	3253-3265/ 10672-10711	ES ₄ ¹	34.66/346.6	88.48	5.31	2.36	0.22	0	0	0.33	0	2.86	9.9/0.99
Tuo168	3088-3112/ 10131-10210	ES ₄ ¹	42.71/427.1	55.43	13.19	15.57	8.79	0	2.95	0.28	0	3.80	16.2/1.62
Tuo71	3148-3195/ 10328-10482	ES ₃ ³	58.69/586.9	80.78	7.06	4.36	1.00	0	4.00	0	0	2.70	15.8/1.58
Tuo71	3578-3613/ 11738-11854	ES ₄ ¹	58.79/587.9	63.86	11.87	11.62	6.00	0	3.00	0	0	3.29	19.3/1.93
Tuo710	3792-3802/ 12440-12474	ES ₄ ¹	48.99/489.9	86.99	7.07	2.35	1.29	0	0	0.38	0	1.92	9.4/0.94
Tuo711	3119-3210/ 10232-10531	ES ₃ ² -ES ₃ ³	26.53/265.3	83.40	8.83	3.94	1.00	0	0	0.22	0	2.71	7.2/0.72
Tuo712	3160-3306/ 10367-10846	ES ₃ ³	53.00/530.0	72.81	11.2	7.92	3.00	0	1.00	0.18	0	3.82	20.2/2.02
Tuo715	3279-3288/ 10757-10787	ES ₃ ³	57.23/572.3	64.71	10.71	12.12	6.00	0	2.00	0	0	3.77	21.6/2.16
Tuo717	2985-2998/ 9793-9836	ES ₃ ²	42.64/426.4	89.28	4.39	2.48	0	0	0	0.28	0	3.00	12.8/1.28
Tuo720	3669-3677/ 12037-12063	ES ₄ ¹	33.95/339.5	73.23	12.84	7.44	2.47	0	0	0.27	2.50	3.00	11.4/1.14

Tuo73	3371-3398/ 11059-11148	ES ₄ ¹	50.87/508.7	76.76	8.49	5.51	2.00	0	3.00	0	0	4.67	23.7/2.37
Tuo74	2964-2966/ 9724-9731	ES ₃ ²	46.65/466.5	84.11	1.53	0.68	0	0	0	0	0	12.19	56.8/5.68
Tuo741	2955-2957/ 9564-9701	ES ₃ ²	46.44/464.4	70.35	6.72	10.38	6.00	2.00	0	0.10	0	4.14	19.2/1.92
Tuo76	3340-3359/ 10959-11020	ES ₄ ¹	51.56/515.6	83.90	3.69	3.34	2.00	0	0	0.70	0	6.28	32.3/3.23
Tuo76	3441-3461/ 11289-11354	ES ₄ ¹	48.22/482.2	80.57	4.33	4.27	3.00	0	1.00	0.67	0	5.65	31.6/3.16
Tuo761	3524-3553/ 11561-11656	ES ₄ ¹	54.23/542.3	83.25	3.28	5.55	2.00	0	1.00	0.29	0	5.19	28.1/2.81
Tuo762	3434-3450/ 11266-11319	ES ₄ ¹	48.32/483.2	74.88	6.51	6.27	3.00	0	2.00	0.15	0	7.46	36.0/3.60

Appendix

Appendix Table 1. Detailed data of $\delta^{18}\text{O}_{\text{‰V-SMOW}}$ values of quartz standard NBS28

No.	$\delta^{18}\text{O}_{\text{‰V-SMOW}}$	No.	$\delta^{18}\text{O}_{\text{‰V-SMOW}}$	No.	$\delta^{18}\text{O}_{\text{‰V-SMOW}}$
1	9.75	24	9.89	47	9.28
2	9.66	25	9.62	48	9.33
3	9.31	26	9.76	49	9.60
4	9.83	27	9.34	50	9.70
5	9.82	28	9.60	51	9.38
6	9.93	29	9.42	52	9.45
7	9.81	30	9.32	53	9.69
8	9.69	31	9.50	54	9.84
9	9.41	32	9.46	55	9.60
10	9.72	33	9.82	56	9.43
11	9.54	34	9.57	57	9.72
12	9.36	35	9.91	58	9.67
13	9.55	36	9.75	59	9.82
14	9.27	37	9.56	60	9.45
15	9.46	38	9.41	61	9.79
16	9.84	39	9.41	62	9.69
17	9.59	40	9.70	63	9.86
18	9.48	41	9.94	64	9.44
19	9.55	42	9.86	65	9.40
20	9.85	43	9.54	66	9.52
21	9.88	44	9.42	67	9.62
22	9.24	45	9.36	68	9.55
23	9.53	46	9.69	69	9.33

Appendix Table 2. Detailed data of $\delta^{18}\text{O}_{\text{‰V-SMOW}}$ values of detrital quartz grains and authigenic quartz overgrowths in four sandstone samples. DQ-detrital quartz, Q1/Q2/Q3-authigenic Q1/Q2/Q3 quartz

No.	Well	Depth, m/ft	$\delta^{18}\text{O}_{\text{‰V-SMOW}}$	NO. of quartz grain	No. of quartz overgrowths relevant to specific grains	Phrases of the analyzed quartz
1	Tuo714	2843.06/9327.62	9.26	1	-	DQ
2	Tuo714	2843.06/9327.62	23.89	1	1	Q1
3	Tuo714	2843.06/9327.62	23.84	1	1	Q1
4	Tuo714	2843.06/9327.62	23.60	1	1	Q1
5	Tuo714	2843.06/9327.62	23.87	1	1	Q1
6	Tuo714	2843.06/9327.62	23.78	1	1	Q1
7	Tuo714	2843.06/9327.62	22.51	1	1	Q1
8	Tuo714	2843.06/9327.62	22.47	1	2	Q1
9	Tuo714	2843.06/9327.62	23.26	1	3	Q2
10	Tuo714	2843.06/9327.62	11.79	1	-	DQ
11	Tuo714	2843.06/9327.62	23.39	1	4	Q1
12	Tuo714	2843.06/9327.62	23.06	1	4	Q1
13	Tuo714	2843.06/9327.62	9.66	2	-	DQ
14	Tuo714	2843.06/9327.62	10.50	2	-	DQ
15	Tuo714	2843.06/9327.62	9.43	2	-	DQ
16	Tuo714	2843.06/9327.62	11.62	2	-	DQ
17	Tuo714	2843.06/9327.62	23.19	3	1	Q1
18	Tuo714	2843.06/9327.62	8.30	3	-	DQ
19	Tuo714	2843.06/9327.62	23.69	3	2	Q1
20	Tuo714	2843.06/9327.62	23.08	3	2	Q1
21	Tuo714	2843.06/9327.62	8.95	4	-	DQ
22	Tuo714	2843.06/9327.62	9.75	4	-	DQ
23	Tuo714	2843.06/9327.62	8.85	4	-	DQ
24	Tuo714	2843.06/9327.62	9.58	4	-	DQ
25	Tuo714	2843.06/9327.62	8.97	4	-	DQ
26	Tuo714	2843.06/9327.62	8.62	4	-	DQ
27	Tuo714	2843.06/9327.62	8.91	5	-	DQ
28	Tuo714	2843.06/9327.62	23.35	5	1	Q1
29	Tuo714	2843.06/9327.62	23.52	5	1	Q1+Q2
30	Tuo714	2843.06/9327.62	23.95	6	1	Q1
31	Tuo714	2843.06/9327.62	8.29	1	-	DQ
32	Tuo714	2843.06/9327.62	23.52	1	1	Q1
33	Tuo714	2843.06/9327.62	22.71	1	1	Q1+DQ
34	Tuo714	2843.06/9327.62	23.16	1	1	Q1
35	Tuo714	2843.06/9327.62	23.27	1	2	Q1+Q2
36	Tuo714	2843.06/9327.62	24.01	1	2	Q1
37	Tuo714	2843.06/9327.62	23.11	1	2	Q1

38	Tuo714	2843.06/9327.62	10.56	2	-	DQ
39	Tuo714	2843.06/9327.62	9.54	2	-	DQ
40	Tuo714	2843.06/9327.62	12.44	3	-	DQ+Q1
41	Tuo714	2843.06/9327.62	20.21	3	-	DQ+Q1
42	Tuo714	2843.06/9327.62	14.83	3	-	DQ+Q1
43	Tuo714	2843.06/9327.62	9.54	3	-	DQ
44	Tuo168	3110.1/10203.74	9.03	1	-	DQ
45	Tuo168	3110.1/10203.74	23.08	1	1	Q2
46	Tuo168	3110.1/10203.74	19.62	1	-	DQ+Q2
47	Tuo168	3110.1/10203.74	10.40	1	-	DQ
48	Tuo168	3110.1/10203.74	12.90	2	-	DQ
49	Tuo168	3110.1/10203.74	12.27	2	-	DQ
50	Tuo168	3110.1/10203.74	12.11	2	-	DQ
51	Tuo168	3110.1/10203.74	12.68	2	-	DQ
52	Tuo168	3110.1/10203.74	19.33	3	1	DQ+Q1
53	Tuo168	3110.1/10203.74	19.02	3	1	DQ+Q1
54	Tuo168	3110.1/10203.74	9.83	3	-	DQ
55	Tuo168	3110.1/10203.74	9.23	4	-	DQ
56	Tuo168	3110.1/10203.74	23.56	4	1	Q2
57	Tuo168	3110.1/10203.74	24.04	4	1	Q2
58	Tuo168	3110.1/10203.74	6.24	5	-	DQ
59	Tuo168	3110.1/10203.74	22.82	5	1	DQ+Q1
60	Tuo168	3110.1/10203.74	22.39	5	1	DQ+Q1
61	Tuo168	3110.1/10203.74	22.88	5	1	DQ+Q1
62	Tuo168	3110.1/10203.74	21.26	5	1	DQ+Q1
63	Tuo168	3110.1/10203.74	23.89	5	1	DQ+Q1
64	Tuo168	3110.1/10203.74	24.32	5	2	Q1
65	Tuo168	3110.1/10203.74	24.99	5	2	Q2
66	Tuo168	3110.1/10203.74	24.33	5	2	Q1
67	Tuo168	3110.1/10203.74	24.86	6	1	Q2
68	Tuo168	3110.1/10203.74	24.64	6	1	Q2
69	Tuo168	3110.1/10203.74	24.67	6	1	Q2
70	Tuo168	3110.1/10203.74	24.67	6	1	Q1
71	Tuo168	3110.1/10203.74	9.30	6	-	DQ
72	Tuo168	3110.1/10203.74	9.01	6	-	DQ
73	Tuo76	3465.25/11368.93	22.98	1	1	Q1
74	Tuo76	3465.25/11368.93	23.69	1	1	Q1
75	Tuo76	3465.25/11368.93	24.19	1	1	Q1
76	Tuo76	3465.25/11368.93	23.13	2	1	Q1
77	Tuo76	3465.25/11368.93	23.75	2	1	Q1
78	Tuo76	3465.25/11368.93	24.03	2	2	Q1
79	Tuo76	3465.25/11368.93	24.35	2	2	Q1
80	Tuo76	3465.25/11368.93	9.58	2	-	DQ
81	Tuo76	3465.25/11368.93	9.72	3	-	DQ
82	Tuo76	3465.25/11368.93	9.94	3	-	DQ

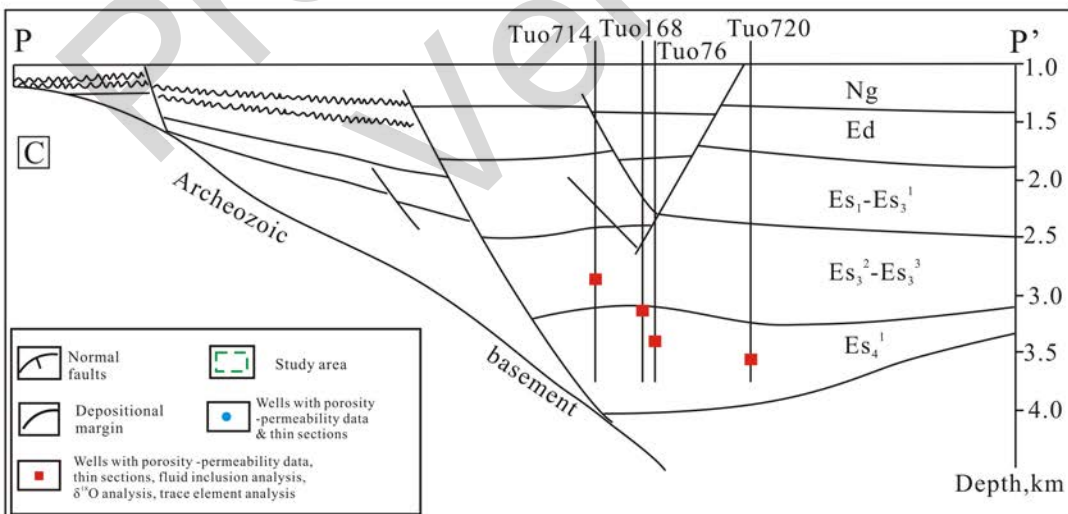
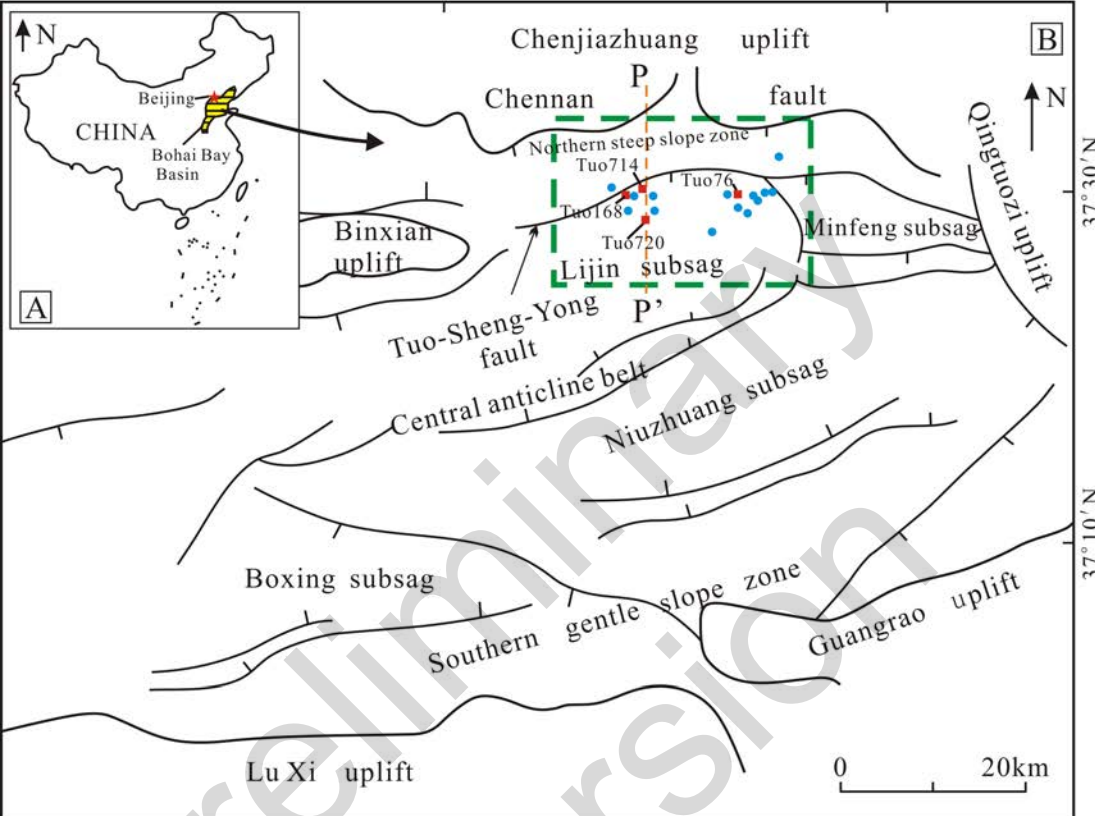
83	Tuo76	3465.25/11368.93	10.02	3	-	DQ
84	Tuo76	3465.25/11368.93	9.09	3	-	DQ
85	Tuo76	3465.25/11368.93	9.23	4	-	DQ
86	Tuo76	3465.25/11368.93	23.76	1	1	Q1
87	Tuo76	3465.25/11368.93	23.22	1	1	Q1
88	Tuo76	3465.25/11368.93	23.97	2	1	Q1
89	Tuo76	3465.25/11368.93	23.09	2	1	Q1
90	Tuo76	3465.25/11368.93	23.19	2	1	Q1
91	Tuo76	3465.25/11368.93	23.58	2	1	Q1
92	Tuo76	3465.25/11368.93	23.30	3	1	Q1
93	Tuo76	3465.25/11368.93	9.50	3	-	DQ
94	Tuo76	3465.25/11368.93	23.90	4	1	Q1
95	Tuo76	3465.25/11368.93	23.22	5	1	Q1
96	Tuo76	3465.25/11368.93	9.44	5	-	DQ
97	Tuo76	3465.25/11368.93	9.29	6	-	DQ
98	Tuo76	3465.25/11368.93	23.17	6	1	Q1
99	Tuo76	3465.25/11368.93	8.55	6	-	DQ
100	Tuo76	3465.25/11368.93	10.01	7	-	DQ
101	Tuo720	3535.00/11597.77	22.75	1	1	Q2
102	Tuo720	3535.0/11597.77	22.54	1	1	Q2
103	Tuo720	3535.0/11597.77	21.19	1	1	DQ+Q2
104	Tuo720	3535.0/11597.77	22.02	1	1	DQ+Q2
105	Tuo720	3535.0/11597.77	21.67	1	1	DQ+Q2
106	Tuo720	3535.0/11597.77	21.28	1	1	DQ+Q2
107	Tuo720	3535.0/11597.77	22.48	1	1	Q2
108	Tuo720	3535.0/11597.77	22.48	1	1	Q3
109	Tuo720	3535.0/11597.77	9.13	1	-	DQ
110	Tuo720	3535.0/11597.77	21.77	2	1	DQ+Q2
111	Tuo720	3535.0/11597.77	22.03	2	1	Q2
112	Tuo720	3535.00/11597.77	22.99	2	1	Q2
113	Tuo720	3535.0/11597.77	22.50	2	1	Q2
114	Tuo720	3535.0/11597.77	22.95	2	1	Q2
115	Tuo720	3535.0/11597.77	22.76	2	1	Q2
116	Tuo720	3535.0/11597.77	22.59	2	1	Q2
117	Tuo720	3535.0/11597.77	22.44	2	1	Q2
118	Tuo720	3535.0/11597.77	9.58	2	-	DQ
119	Tuo720	3535.0/11597.77	22.44	3	1	Q1
120	Tuo720	3535.0/11597.77	22.52	3	1	Q1
121	Tuo720	3535.0/11597.77	7.16	3	-	DQ
122	Tuo720	3535.0/11597.77	8.77	4	-	DQ
123	Tuo720	3535.00/11597.77	8.03	4	-	DQ
124	Tuo720	3535.0/11597.77	11.98	4	-	DQ
125	Tuo720	3535.0/11597.77	8.01	4	-	DQ
126	Tuo720	3535.0/11597.77	8.07	4	-	DQ
127	Tuo720	3535.0/11597.77	9.36	4	-	DQ

128	Tuo720	3535.0/11597.77	8.45	4	-	DQ
129	Tuo720	3535.0/11597.77	10.28	4	-	DQ
130	Tuo720	3535.0/11597.77	10.20	4	-	DQ
131	Tuo720	3535.0/11597.77	8.24	4	-	DQ
132	Tuo720	3535.0/11597.77	21.04	5	1	DQ+Q2
133	Tuo720	3535.0/11597.77	22.52	5	1	Q2
134	Tuo720	3535.00/11597.77	21.92	5	1	DQ+Q2
135	Tuo720	3535.0/11597.77	21.63	5	1	DQ+Q2
136	Tuo720	3535.0/11597.77	22.85	5	1	Q2
137	Tuo720	3535.0/11597.77	13.49	5	1	DQ+Q2
138	Tuo720	3535.0/11597.77	22.33	5	2	Q2
139	Tuo720	3535.0/11597.77	9.85	5	-	DQ
140	Tuo720	3535.0/11597.77	17.35	5	2	DQ+Q2
141	Tuo720	3535.0/11597.77	8.99	5	-	DQ
142	Tuo720	3535.0/11597.77	22.27	6	1	Q1
143	Tuo720	3535.0/11597.77	23.25	6	1	Q2
144	Tuo720	3535.0/11597.77	22.44	6	1	Q2
145	Tuo720	3535.00/11597.77	21.42	6	1	Q1
146	Tuo720	3535.0/11597.77	23.14	6	1	Q2
147	Tuo720	3535.0/11597.77	9.46	6	-	DQ
148	Tuo720	3535.0/11597.77	8.92	6	-	DQ
149	Tuo720	3535.0/11597.77	20.10	6	-	DQ+Q1
150	Tuo720	3535.0/11597.77	23.31	6	2	Q1
151	Tuo720	3535.0/11597.77	22.69	6	2	Q1
152	Tuo720	3535.0/11597.77	22.55	6	2	Q1
153	Tuo720	3535.0/11597.77	23.02	6	2	Q1
154	Tuo720	3535.0/11597.77	22.39	6	2	Q1
155	Tuo720	3535.0/11597.77	22.53	6	3	Q2
156	Tuo720	3535.00/11597.77	23.15	6	3	Q2
157	Tuo720	3535.0/11597.77	23.32	6	3	Q2
158	Tuo720	3535.0/11597.77	21.72	7	1	Q3
159	Tuo720	3535.0/11597.77	22.40	7	1	Q2
160	Tuo720	3535.0/11597.77	22.65	7	1	Q2
161	Tuo720	3535.0/11597.77	21.86	7	1	Q1
162	Tuo720	3535.0/11597.77	9.03	7	-	DQ
163	Tuo720	3535.0/11597.77	22.91	7	1	Q3
164	Tuo720	3535.0/11597.77	20.81	8	1	DQ+Q1
165	Tuo720	3535.0/11597.77	22.77	8	1	Q1
166	Tuo720	3535.0/11597.77	9.98	8	-	DQ
167	Tuo720	3535.00/11597.77	20.43	1	-	DQ+Q1
168	Tuo720	3535.0/11597.77	23.45	1	1	Q1
169	Tuo720	3535.0/11597.77	9.90	2	-	DQ
170	Tuo720	3535.0/11597.77	9.55	2	-	DQ
171	Tuo720	3535.0/11597.77	10.29	3	-	DQ
172	Tuo720	3535.0/11597.77	9.61	3	-	DQ

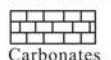
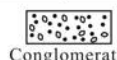
173	Tuo720	3535.0/11597.77	9.60	3	-	DQ
174	Tuo720	3535.0/11597.77	9.56	3	-	DQ
175	Tuo720	3535.0/11597.77	21.32	4	1	DQ+Q2
176	Tuo720	3535.0/11597.77	22.98	4	1	Q2
177	Tuo720	3535.0/11597.77	21.14	4	1	DQ+Q2
178	Tuo720	3535.00/11597.77	21.31	4	1	DQ+Q2
179	Tuo720	3535.0/11597.77	8.61	4	-	DQ
180	Tuo720	3535.0/11597.77	20.31	5	1	DQ+Q2
181	Tuo720	3535.0/11597.77	22.62	5	1	Q2
182	Tuo720	3535.0/11597.77	22.75	5	1	Q3
183	Tuo720	3535.0/11597.77	8.70	5	-	DQ
184	Tuo720	3535.0/11597.77	22.77	5	2	Q2
185	Tuo720	3535.0/11597.77	22.26	5	2	Q1
186	Tuo720	3535.0/11597.77	8.92	5	-	DQ
187	Tuo720	3535.0/11597.77	22.27	6	1	Q2
188	Tuo720	3535.0/11597.77	22.69	6	1	Q2
189	Tuo720	3535.0/11597.77	22.59	6	2	Q1
190	Tuo720	3535.0/11597.77	22.65	6	2	Q1
191	Tuo720	3535.0/11597.77	22.78	6	2	Q1
192	Tuo720	3535.0/11597.77	22.81	6	2	Q1
193	Tuo720	3535.0/11597.77	22.80	6	2	Q1
194	Tuo720	3535.0/11597.77	14.07	6	-	DQ+Q1
195	Tuo720	3535.0/11597.77	8.66	6	-	DQ
196	Tuo720	3535.0/11597.77	8.78	6	-	DQ
197	Tuo720	3535.0/11597.77	19.91	6	3	DQ+Q1

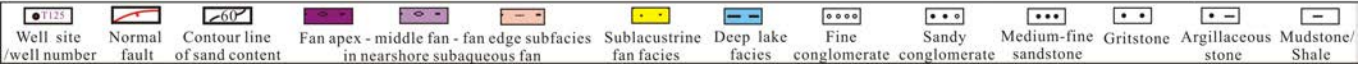
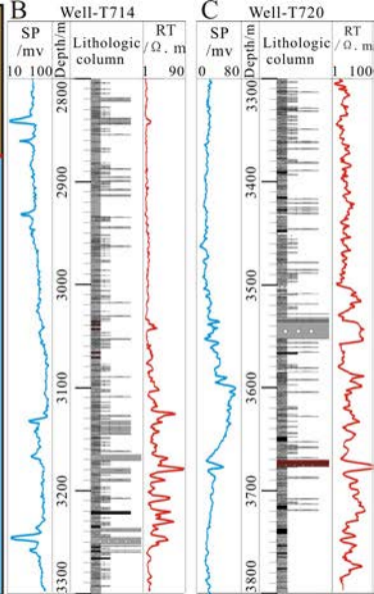
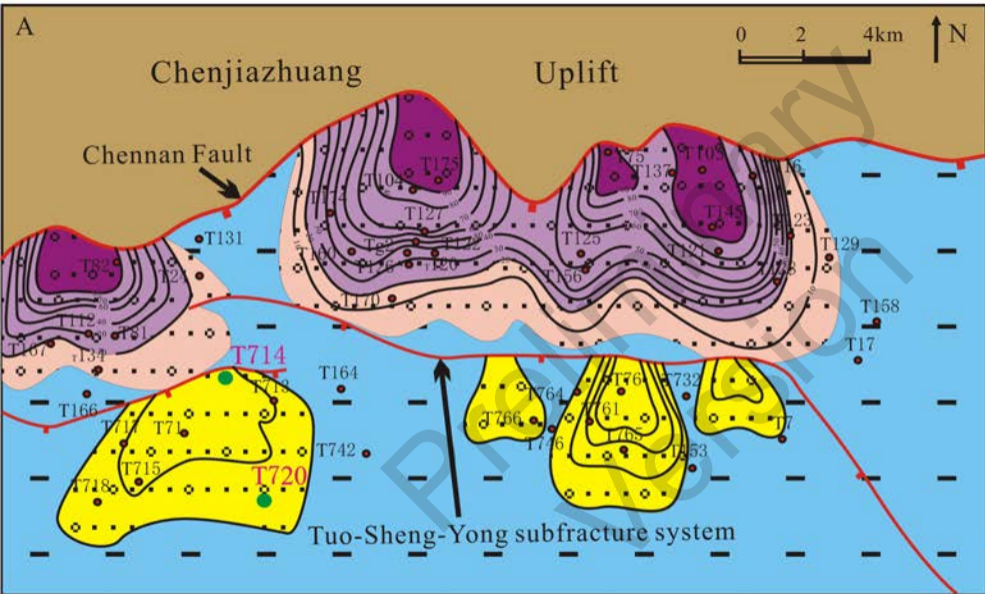
118° 10' E

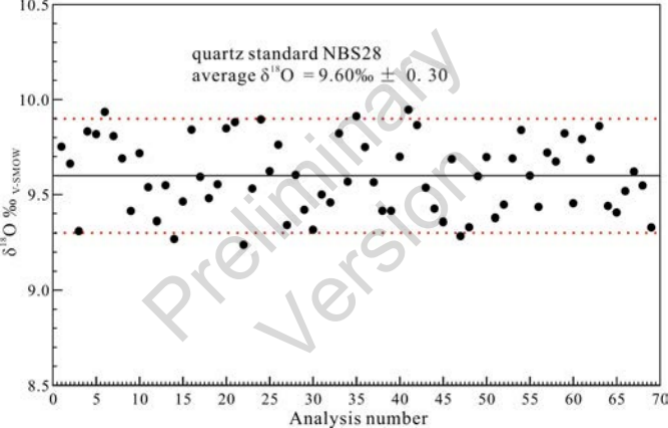
118° 50' E










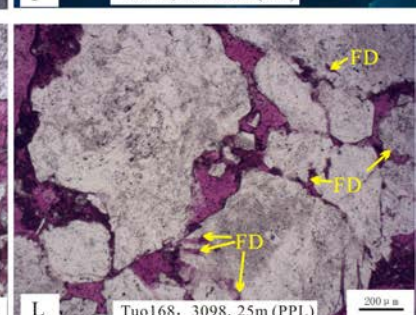
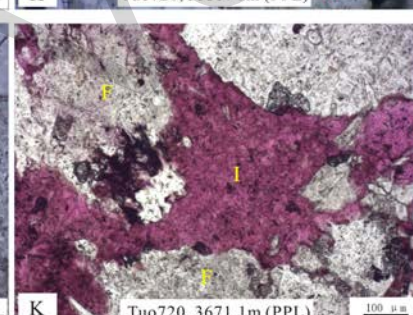
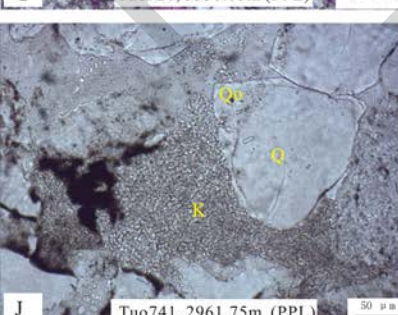
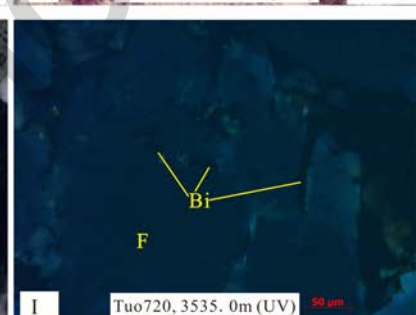
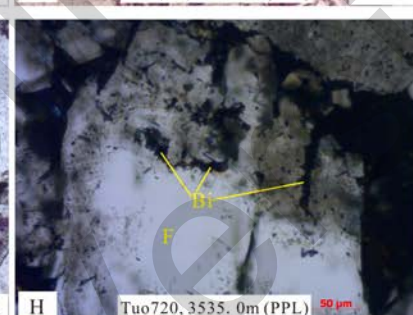
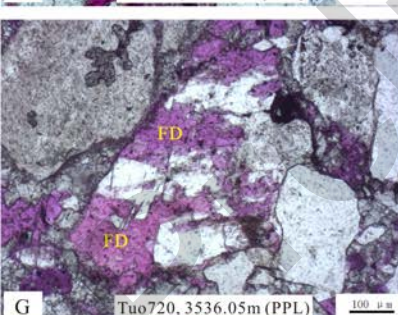
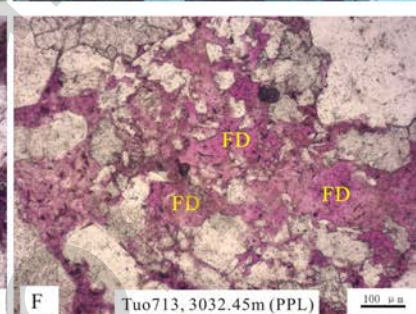
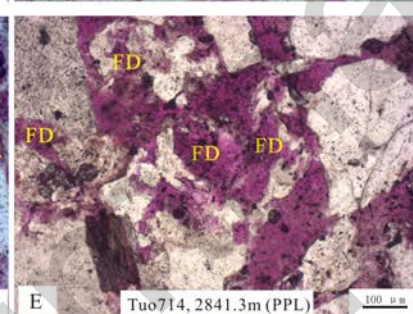
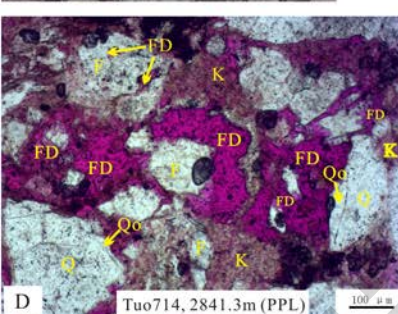
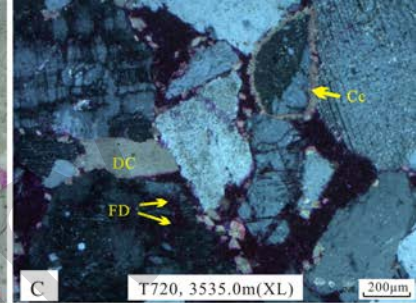
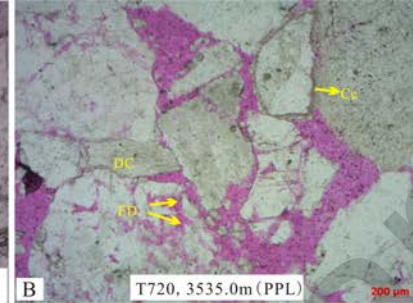
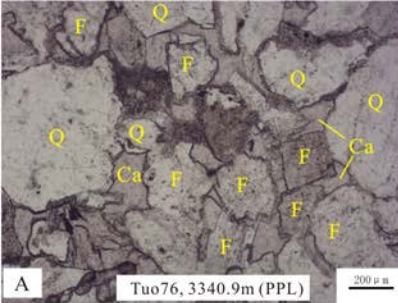
System	Series	Stratigraphy			Age (Ma)	Thickness (m)	Lithology	Sedimentary environment	Main source rocks	Reservoir rocks	Seal rocks	Tectonic evolution
		Formation	Member	Sub-Member								
Quaternary		Pingyuan (Qp)				100-230		Floodplain				Postrift Stage
Neogene	Pliocene	Minghuazhen(Nm)				600-900		Floodplain				
		Miocene	Guangtao (Ng)	Ng ^u	5.1	300-400		Braided stream				
Ng ^l												
Paleogene	Oligocene	Dongying (Ed)	Ed1	24.6	0-110		Deltaic				Stage IV	
			Ed2	28.1	0-280		Deltaic Lacustrine					
			Ed3	32.8	0-420		Deltaic Lacustrine					
		Shahejie (Es)	Es1	32.8	0-450		Deltaic Lacustrine					
			Es2	38.0	0-350		Deltaic Fluvial					
			Es3	Es ₃ ¹	100-300		Deltaic Fluvial					
	Es ₃ ²	200-500			Fan delta Subaqueous fan							
	Es ₃ ³	200-600			Deep-water fan Lacustrine							
	Eocene	Es4	Es ₄ ¹	42.5	300-700		Subaqueous fan Deep-water fan					
			Es ₄ ²	200-800		Salt lake						
			Paleocene	Kongdian (Ek)	Ek1	52.0	0-1300		Fluvial Salt lake			
	Ek2	0-900				Fluvial Lacustrine						
Ek3	65.0											

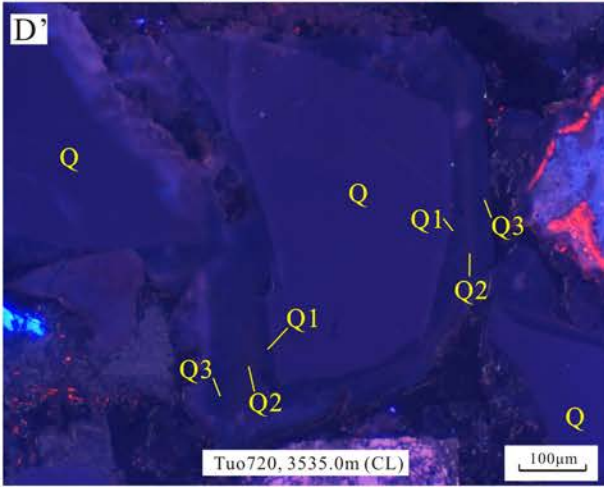
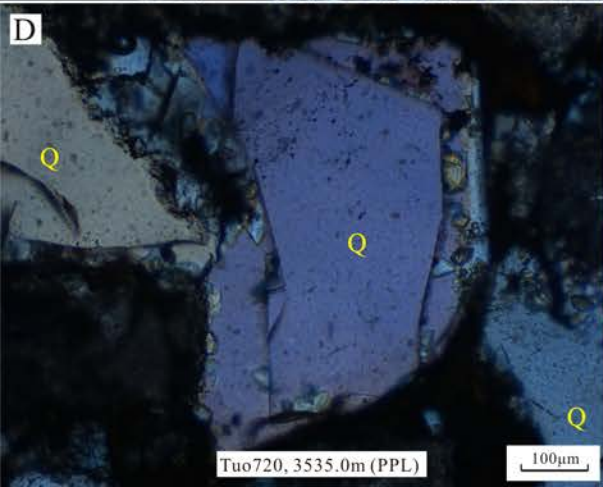
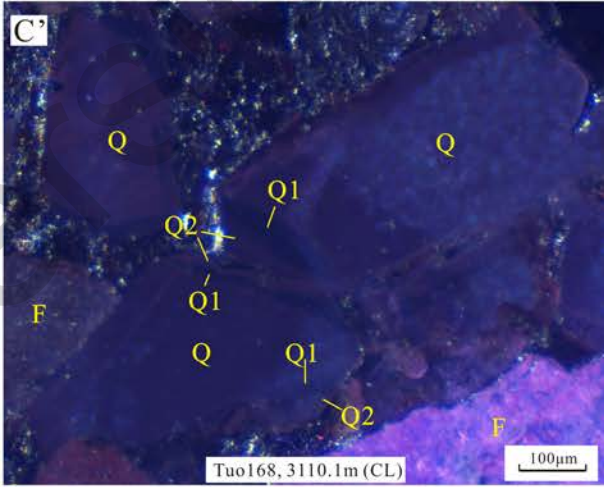
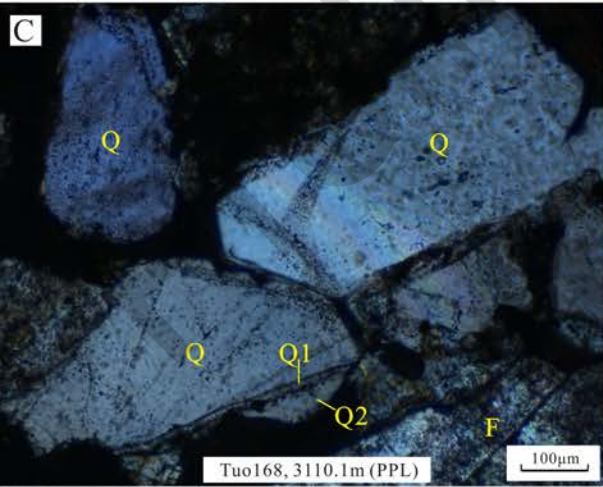
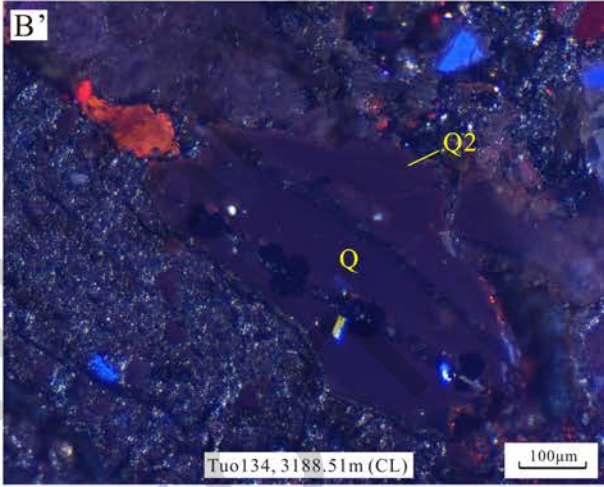
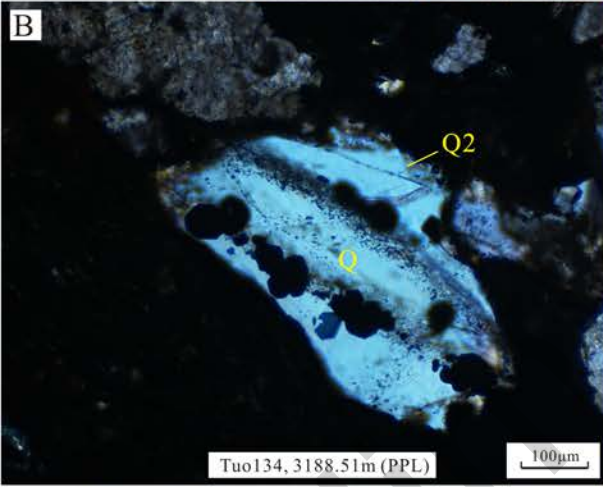
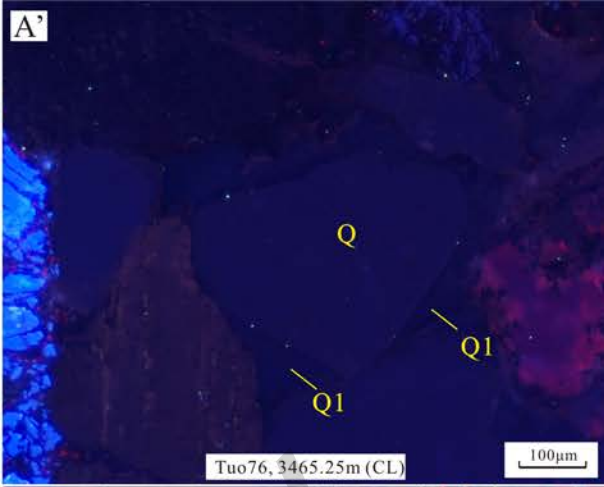
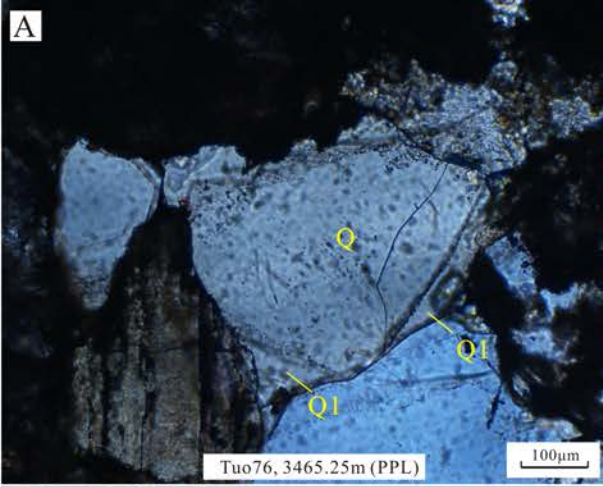


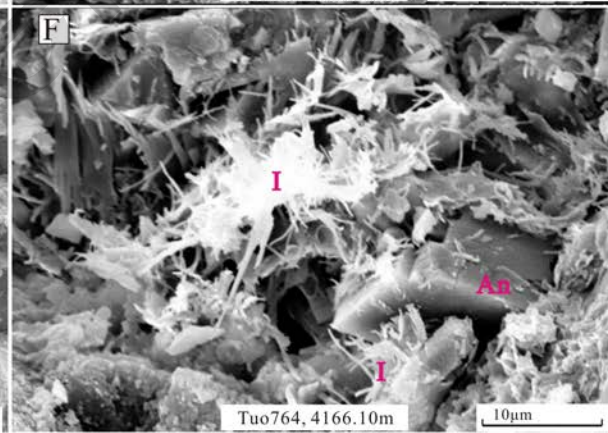
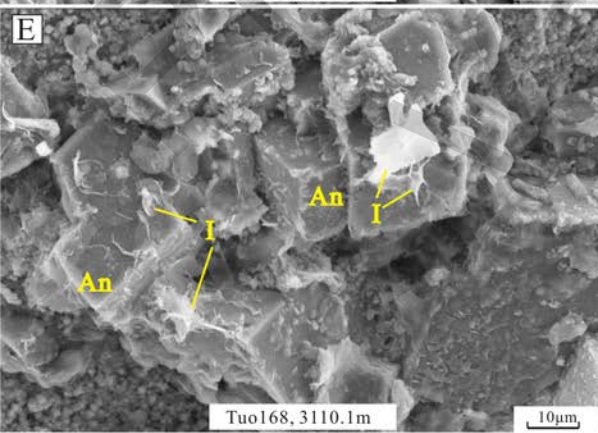
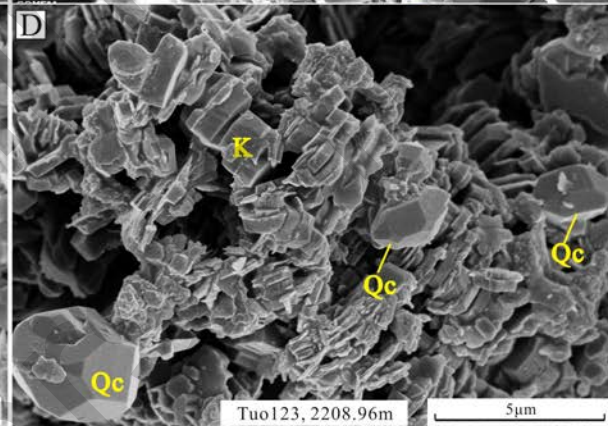
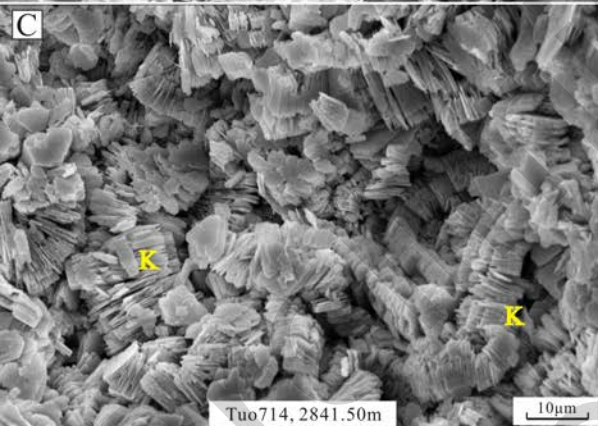
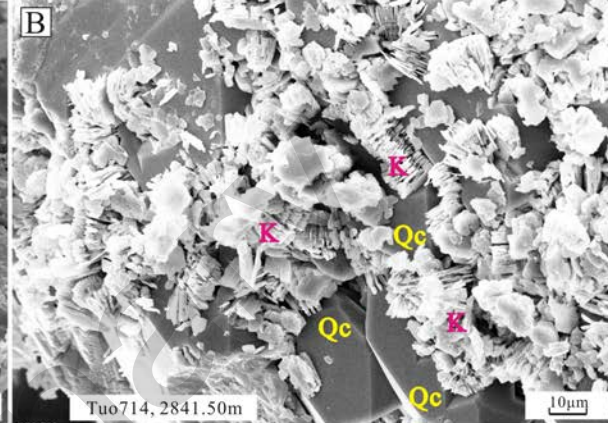
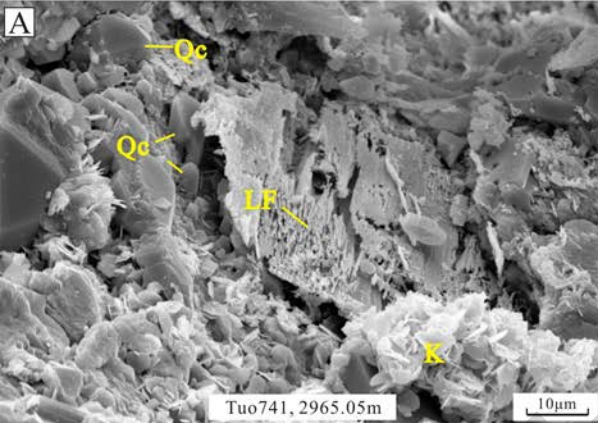


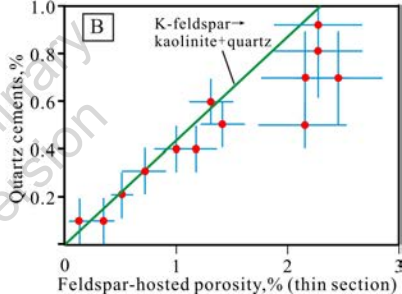
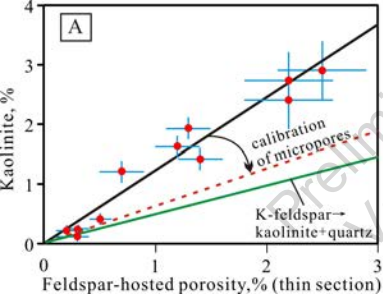


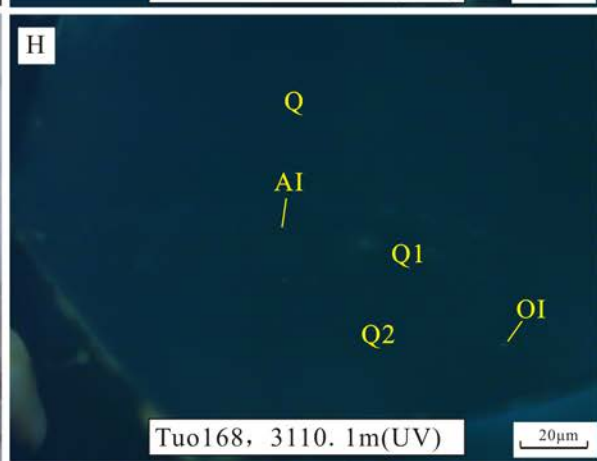
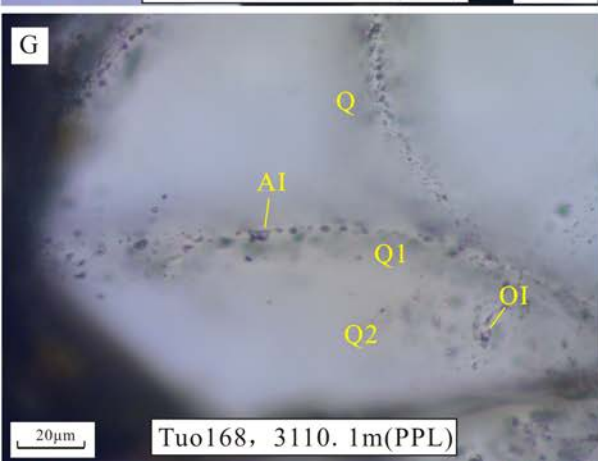
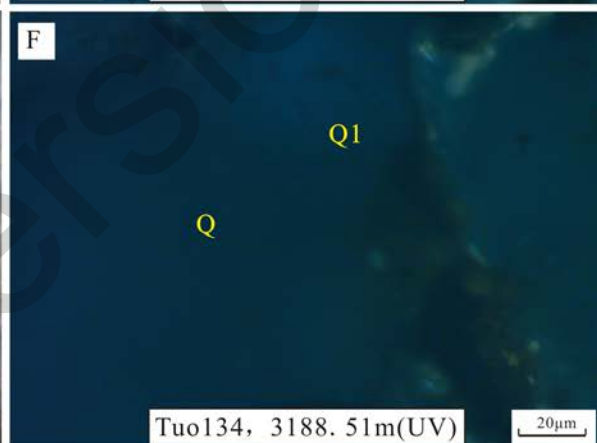
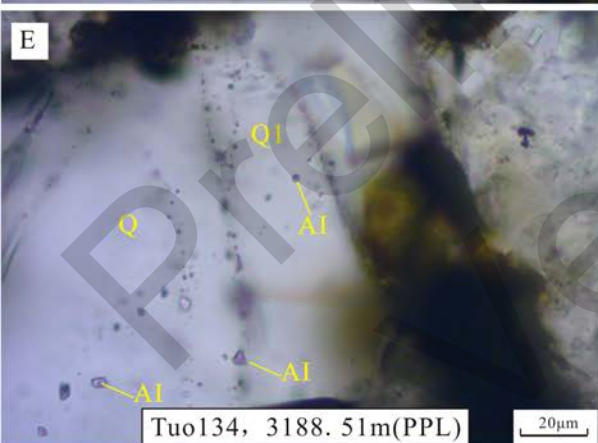
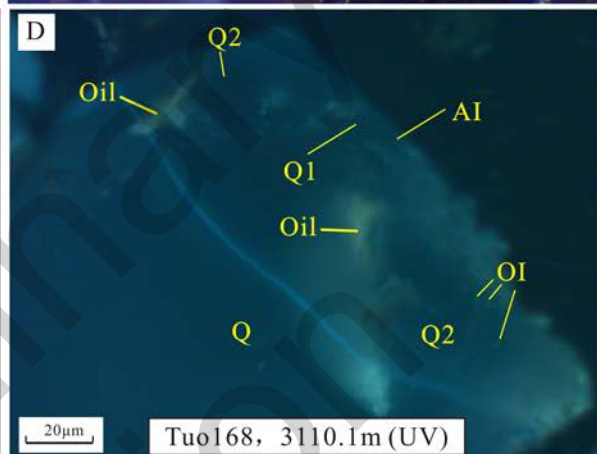
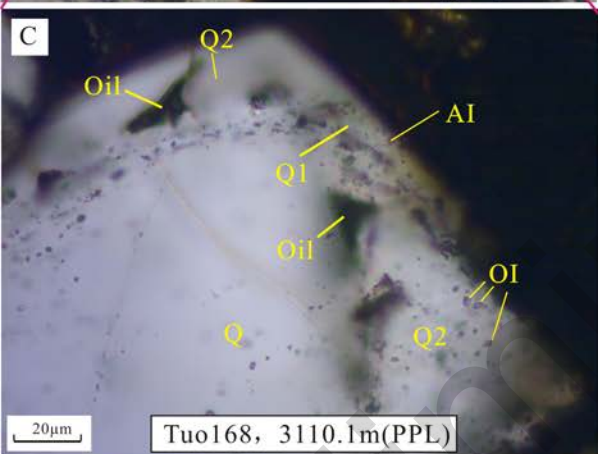
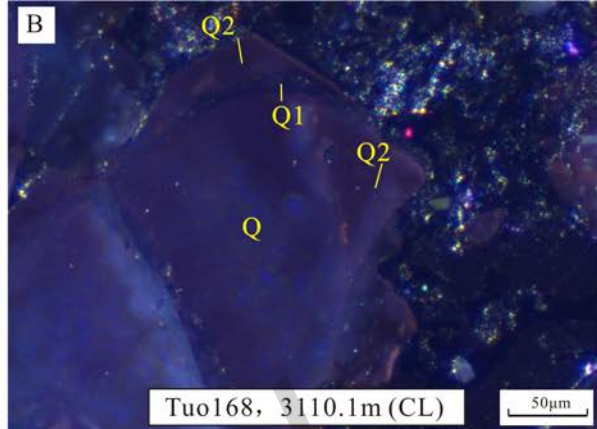
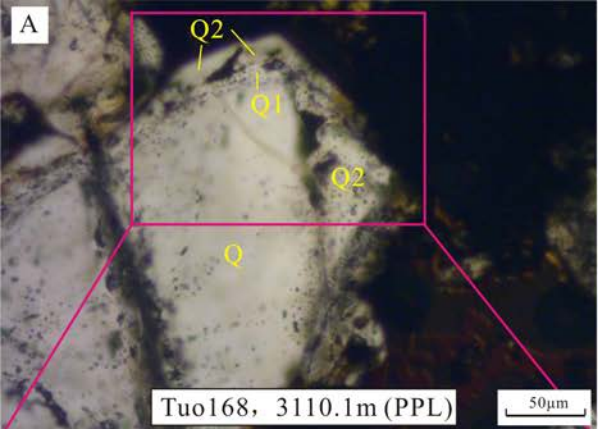
Diagenesis	Eodiagenesis	Mesodiagenesis
Compaction		
Calcite/Dolomite cementation		
Feldspar dissolution		
Authigenic kaolinite precipitation		
Quartz overgrowth cementation		
Ankerite/Ferrocalsite cementation		
Authigenic illite precipitation		

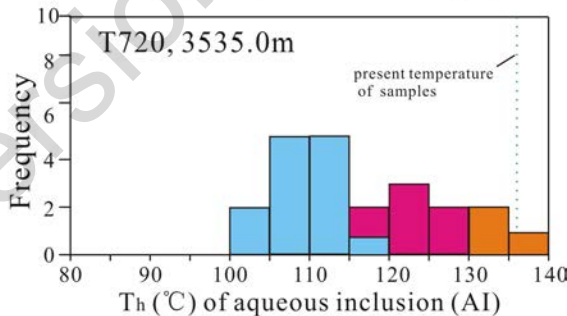
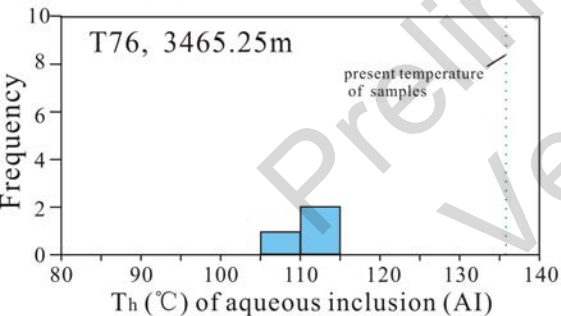
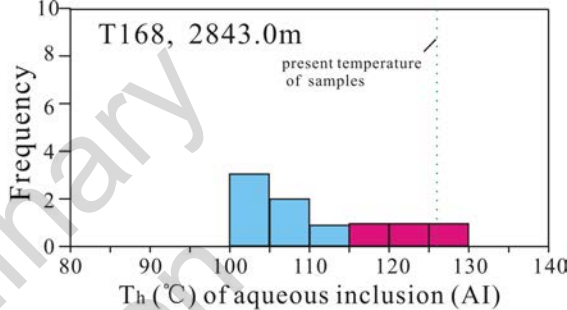
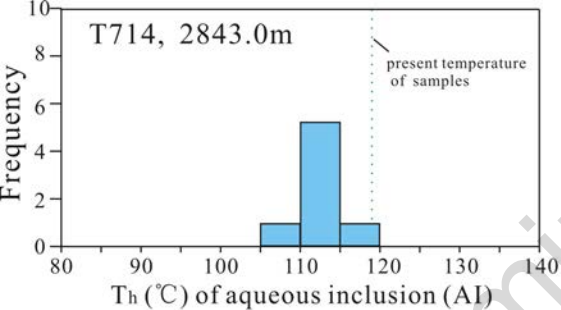












AI in Q1 quartz

AI in Q2 quartz

AI in Q3 quartz

